

A space-time high-order implicit shock tracking method for shock-dominated unsteady flows

Charles Naudet^{a,1}, Matthew J. Zahr^{a,2,*}

^aDepartment of Aerospace and Mechanical Engineering, University of Notre Dame, Notre Dame, IN 46556, United States

Abstract

High-order implicit shock tracking (fitting) is a class of high-order, optimization-based numerical methods to approximate solutions of conservation laws with non-smooth features by aligning elements of the computational mesh with non-smooth features. This ensures the non-smooth features are perfectly represented by inter-element jumps and high-order basis functions approximate smooth regions of the solution without nonlinear stabilization, which leads to accurate approximations on traditionally coarse meshes. In this work, we extend implicit shock tracking to time-dependent problems using a slab-based space-time approach. This is achieved by reformulating a time-dependent conservation law as a steady conservation law in one higher dimension and applying existing implicit shock tracking techniques. To avoid computations over the entire time domain and unstructured mesh generation in higher dimensions, we introduce a general procedure to generate conforming, simplex-only meshes of space-time slabs in such a way that preserves features (e.g., curved elements, refinement regions) from previous time slabs. The use of space-time slabs also simplifies the shock tracking problem by reducing temporal complexity. Several practical adaptations of the implicit shock tracking solvers are developed for the space-time setting including 1) a self-adjusting temporal boundary, 2) nondimensionalization of a space-time slab, 3) adaptive mesh refinement, and 4) shock boundary conditions, which lead to accurate solutions on coarse space-time grids, even for problem with complex flow features such as curved shocks, shock formation, shock-shock and shock-boundary interaction, and triple points.

Keywords: Shock tracking, shock fitting, high-order methods, discontinuous Galerkin, high-speed flows, space-time methods

1. Introduction

Shock-dominated flows commonly arise in science and engineering disciplines including supersonic and hypersonic aerodynamics, astrophysics, oceanic wave modeling, radiation hydrodynamics, and many others. Despite their prevalence, accurate and robust simulation of shock-dominated flows remains a significant challenge for modern computational fluid dynamics methods, which becomes more significant as the strength of shocks increase. High-order methods, such as discontinuous Galerkin (DG) methods [9, 18], have received considerable attention because they are highly accurate per degree of freedom and introduce minimal dissipation, and have been shown to provide higher fidelity solutions for problems with propagating waves, turbulent field flow, nonlinear interactions, and multiple scales [54]. DG offers additional advantages such as geometric flexibility and a high degree of parallel scalability. Despite these advantages, high-order methods are known to lack robustness for shock-dominated flows because high-order approximation of shocks and contact discontinuities leads to spurious oscillations that cause a breakdown of numerical solvers.

The most popular class of methods to suppress these oscillations is known as *shock capturing*, which includes limiting [48, 4], reconstruction [16, 27], and artificial viscosity [33, 3] approaches. These methods reduce the order of accuracy of the method near discontinuities, and therefore globally, to first-order, which reduces the accuracy per degree of freedom of the underlying method. This loss of accuracy is usually

*Corresponding author

Email addresses: cnaudet@nd.edu (Charles Naudet), mzahr@nd.edu (Matthew J. Zahr)

¹Graduate Student, Department of Aerospace and Mechanical Engineering, University of Notre Dame

²Assistant Professor, Department of Aerospace and Mechanical Engineering, University of Notre Dame

remedied by aggressive h -refinement, particularly in the vicinity of discontinuities. While these methods have been shown to solve complex flows, their robustness is inherently tied to an interplay between the amount of dissipation added to smear discontinuities and the grid fineness, and their accuracy will always be limited to first-order due to the smooth approximation of discontinuous features. Furthermore, these methods are susceptible to disturbances such as surface anomalies [15, 14, 7], spurious oscillations [25, 8], and carbuncles [37, 32, 38].

An alternative approach, known as *shock tracking* or *shock fitting*, adjusts the computational mesh to align faces of mesh elements with discontinuities in the solution. This allows the discontinuities to be represented perfectly with the inter-element jump in the solution basis without the need of additional stabilization, which recovers the high accuracy per degree of freedom of high-order methods and avoids disturbances. However, this is a difficult meshing problem that requires generating a fitted mesh to the (unknown) shock surface. Many previous approaches employ specialized formulations and solvers which are dimension dependent and do not easily generalize [17, 13, 6] and/or are limited to relatively simple problems [44, 45, 49]. One noteworthy class of methods is explicit shock tracking, surveyed in [31, 40], which mostly consist of explicitly identifying the shock and using the Rankine-Hugoniot conditions to compute its motion and upstream/downstream states. These methods are not easily applicable to discontinuities whose topologies are not known *a priori* or undergo substantial shock motion, making them ill-suited for many important phenomena including curved shocks, shock intersections, shock formation, and shock-boundary interactions.

A new class of high-order methods, known as *implicit shock tracking*, has recently emerged, which includes the Moving Discontinuous Galerkin Method with Interface Condition Enforcement (MDG-ICE) [10, 22, 23] and High-Order Implicit Shock Tracking (HOIST) [56, 59, 20] methods. Like traditional shock tracking, these methods aim to align element faces with discontinuities in the flow to recover high accuracy per degree of freedom without stabilization and avoid nonlinear instabilities. However, instead of attempting to explicitly mesh the unknown discontinuity surface, they discretize the conservation law on a mesh without knowledge of discontinuities and solve an optimization problem over the discrete solution variables and nodal coordinates of the mesh. The solution of this optimization problem is a discontinuity-aligned mesh and the solution of the discretized conservation law. This critical innovation has led to a general approach that has been shown to handle complex shock phenomena including curved and reflected shocks, shock formation, and shock-shock interaction for viscous and inviscid, inert and reacting flows of varying degree of complexity [10, 23, 59, 58, 20].

Implicit shock tracking methods are formulated in terms of *steady* conservation laws and have been predominately applied to steady problems or unsteady problems using a space-time formulation that converts an unsteady conservation law to a steady conservation law in one higher dimension (usually coupling the entire temporal domain). An exception is [41] where the HOIST method is embedded in a method of lines temporal discretization that solves a steady shock tracking problem at each time step. As noted in [41, 42], this approach suffers from similar limitations as explicit shock fitting methods; in particular, it is most suitable for problems with limited shock motion and cannot handle shock-shock or shock-boundary interactions without complex mesh modifications. Space-time formulations [29, 46, 24] do not suffer from these limitations because propagating shocks manifest as stationary discontinuity surfaces in space-time and shock intersection are simply triple points in space-time.

In this work, we develop a slab-based space-time shock tracking approach based on the HOIST method to track complex shock dynamics with a computational grid without coupling the entire temporal domain. Our work is similar to [11] that demonstrated the MDG-ICE method in a slab-based space-time setting. The contributions of our work are:

- systematic formulation of a traditional conservation law where the spatial and temporal independent variables are treated separately as a steady conservation law in one higher dimension with special care given to the relationship between the space-time terms (flux function, source term, numerical flux function) and the corresponding term from the spatial formulation;
- a general procedure to generate and refine a conforming, simplex-only mesh of a space-time slab in such a way that preserves features (e.g., curved elements, refinement regions, tracked discontinuities) from the previous time slab;
- formulation of the HOIST method over a space-time slab; and
- practical adaptations of the HOIST for the space-time setting including a self-adjusting temporal

boundary (first introduced in [11]), nondimensionalization of space-time slab, adaptive mesh refinement, and shock boundary conditions whereby boundary conditions are directly applied to shocks and upstream elements are removed from the space-time mesh (if the upstream state is known) [19].

The remainder of this paper is organized as follows. Section 2 systematically builds up a space-time formulation of a time-dependent conservation law from a traditional formulation that separates the temporal and spatial independent variables, transforms the space-time conservation law to a reference domain such that domain deformations appear explicitly, and details a high-order discontinuous Galerkin discretization of the transformed space-time conservation law. Section 3 introduces our approach to generate conforming, simplex-only meshes of space-time slabs that preserve features (refinement regions, high-order elements, tracked discontinuities) in the previous slab. Section 4 details the extension of the HOIST method to the space-time slab setting. Section 5 shows the proposed method successfully tracks space-time shocks and produces accurate solutions on a series of increasingly complex one- and two-dimensional time-dependent conservation laws, some of which include complicated shock features such as curved shocks, shock-shock and shock-boundary intersections, and shock formation. Finally, Section 6 offers conclusions.

2. Governing equations and high-order discretization

In this section, we introduce a time-dependent system of conservation laws that will be used to model unsteady, shock-dominated flows (Section 2.1) as well as its formulation as a space-time partial differential equation that treats the temporal dimension as another spatial dimension (Section 2.2). Then we recast the space-time conservation law on a fixed reference space-time domain such that deformations to the physical space-time domain appear explicitly in the flux and source term (Section 2.3). Finally, we introduce a DG discretization of the transformed space-time conservation law (Section 2.4). Throughout this section, we emphasize systematic construction of space-time quantities in terms of spatial quantities.

2.1. Time-dependent system of conservation laws

Consider a general system of m hyperbolic partial differential equations posed in the spatial domain $\Omega_x \subset \mathbb{R}^d$ over the time interval $\mathcal{T} := (t_0, t_1) \subset \mathbb{R}_{\geq 0}$

$$\frac{\partial U_x}{\partial t} + \nabla_x \cdot \mathcal{F}_x(U_x) = \mathcal{S}_x(U_x), \quad (1)$$

where $t \in \mathcal{T}$ is the temporal coordinate, $x = (x_1, \dots, x_d) \in \Omega_x$ is the spatial coordinate, $U_x(\cdot, t) : \Omega_x \rightarrow \mathbb{R}^m$ is the conservative state implicitly defined as the solution to (1), $\mathcal{F}_x : \mathbb{R}^m \rightarrow \mathbb{R}^{m \times d}$ with $\mathcal{F}_x : W_x \mapsto \mathcal{F}_x(W_x)$ is the physical flux function where W_x is used to denote the first argument of the physical flux function, $\mathcal{S}_x : \mathbb{R}^m \rightarrow \mathbb{R}^m$ is the physical source term, $(\nabla_x \cdot)$ is the divergence operator on the domain Ω_x defined as $(\nabla_x \cdot \psi)_i := \partial_{x_j} \psi_{ij}$ (summation implied on repeated index), and $\partial\Omega_x$ is the boundary of the spatial domain (with appropriate boundary conditions prescribed). In general, the solution $U(x, t)$ may contain discontinuities, in which case, the conservation law (1) holds away from the discontinuities and the Rankine-Hugoniot conditions hold at discontinuities.

The Jacobian of the projected inviscid flux is

$$B_x : \mathbb{R}^m \times \mathbb{S}_{d'} \rightarrow \mathbb{R}^{m \times m}, \quad B_x : (W_x, \eta_x) \mapsto \frac{\partial[\mathcal{F}_x(W_x)\eta_x]}{\partial W_x}, \quad (2)$$

where $\mathbb{S}_{d'} := \{\eta \in \mathbb{R}^{d'} \mid \|\eta\| = 1\}$ and η_x is the unit normal in the spatial setting. The eigenvalue decomposition of the Jacobian is

$$B_x(W_x, \eta_x) = V_x(W_x, \eta_x) \Lambda_x(W_x, \eta_x) V_x(W_x, \eta_x)^{-1}, \quad (3)$$

where $\Lambda_x : \mathbb{R}^m \times \mathbb{S}_{d'} \rightarrow \mathbb{R}^{m \times m}$ is a diagonal matrix containing the real eigenvalues of B_x and the columns of $V_x : \mathbb{R}^m \times \mathbb{S}_{d'} \rightarrow \mathbb{R}^{m \times m}$ contain the corresponding right eigenvectors. The projected Jacobian is commonly used to define linearized Riemann solvers [26, 47] for the conservation law (1), which in turn is used to define monotonic, upwind numerical flux functions for numerical methods, $\mathcal{H}_x : \mathbb{R}^m \times \mathbb{R}^m \times \mathbb{S}_{d'} \rightarrow \mathbb{R}^m$, as

$$\mathcal{H}_x : (W_x^+, W_x^-, \eta_x) \mapsto \frac{1}{2} (\mathcal{F}_x(W_x^+)\eta_x + \mathcal{F}_x(W_x^-)\eta_x) + \frac{1}{2} \tilde{B}_x(W_x^+, W_x^-, \eta_x)(W_x^+ - W_x^-), \quad (4)$$

where $\tilde{B}_x : \mathbb{R}^m \times \mathbb{R}^m \times \mathbb{S}_{d'} \rightarrow \mathbb{R}^{m \times m}$ is the Jacobian of the linearized Riemann problem [47]. In this work, we use Roe's numerical flux [39] that takes

$$\tilde{B}_x(W_x^+, W_x^-, \eta_x) = \left| B_x(\hat{U}(W_x^+, W_x^-), \eta_x) \right|, \quad (5)$$

where $|B_x| = V_x |\Lambda_x| V_x^{-1}$ is the matrix absolute value of the projected Jacobian and $\hat{U} : \mathbb{R}^m \times \mathbb{R}^m \rightarrow \mathbb{R}^m$ is the equation-specific Roe average.

Remark 1. *The Jacobian of the projected inviscid flux is well-defined for any projection direction using (2); however, in this work, we restrict its definition to unit projection directions ($\mathbb{S}_{d'}$) because the eigenvalue decompositions can be substantially simpler under this assumption. Expressions for the projected Jacobian and its eigenvalue decomposition for the conservation laws considered in this work are provided in Appendix A.*

Remark 2. *Other standard numerical flux functions fit the form in (4). The Vijayasundaram flux [50] uses a linear Riemann problem of the form (4) with the projected Jacobian evaluated at the arithmetic average of the two states $\hat{U}(W_x^+, W_x^-) = (W_x^+ + W_x^-)/2$ and the flux average replaced with the linearized flux average $B_x(\hat{U}(W_x^+, W_x^-), \eta_x) \hat{U}(W_x^+, W_x^-)$ [52]. Furthermore, the local Lax-Friedrichs or Rusanov [47] flux takes the linearized Riemann problem matrix to be*

$$\tilde{B}_x : (W_x^+, W_x^-, \eta_x) \mapsto \max \left\{ \|\Lambda_x(W_x^+, \eta_x)\|_\infty, \|\Lambda_x(W_x^-, \eta_x)\|_\infty \right\} I_m, \quad (6)$$

where $I_m \in \mathbb{R}^{m \times m}$ is the identity matrix.

Remark 3. *Smoothed [59] and entropy-fixed [17] variants of the numerical flux in (4) are obtained by replacing the component-wise absolute value function with a smoothed absolute value or entropy fix.*

2.2. Space-time formulation

The conservation law in (1) describes a general time-dependent system of conservation laws in a d' -dimensional spatial domain. Because the proposed method tracks discontinuities over space-time slabs, we reformulate (1) as a steady conservation law in a space-time domain [29, 46, 24]. To this end, we define the space-time domain as $\Omega := \Omega_x \times \mathcal{T} \subset \mathbb{R}^d$ ($d = d' + 1$) with boundary $\partial\Omega$, and let $z = (x, t) \in \Omega$ denote the space-time coordinate. Because the space-time domain is a Cartesian product of the spatial domain with a time interval, we will refer to it as a *space-time slab*. The boundary of a space-time slab $\partial\Omega$ consists of three pieces: 1) the spatial boundary, $\partial\Omega_x \times \mathcal{T}$, 2) the bottom of the slab, $\Omega_x \times \{t_0\}$, and 3) the top of the slab, $\Omega_x \times \{t_1\}$. Without loss of generality, we formulate the space-time conservation law, as well as its transformation and discretization (Section 2.4) over a single arbitrary slab corresponding to the time interval \mathcal{T} ; in practice, we use a sequence of space-time slabs to cover the temporal domain of interest.

The conservation law in (1) can be written as a steady conservation law over the space-time slab as

$$\nabla \cdot \mathcal{F}(U) = \mathcal{S}(U), \quad (7)$$

where $U : \Omega \rightarrow \mathbb{R}^m$ is the space-time conservative vector implicitly defined as the solution of (7) and related to the solution of the spatial conservation law as $U : z \mapsto U_x(x, t)$, $\mathcal{F} : \mathbb{R}^m \rightarrow \mathbb{R}^{m \times d}$ and $\mathcal{S} : \mathbb{R}^m \rightarrow \mathbb{R}^m$ are the space-time flux function and source term, respectively, and related to the spatial conservation law terms as

$$\mathcal{F} : W \mapsto [\mathcal{F}_x(W) \quad W], \quad \mathcal{S} : W \mapsto \mathcal{S}_x(W), \quad (8)$$

and $(\nabla \cdot)$ is the space-time divergence operator defined as $\nabla \cdot [\psi \quad \phi] = \nabla_x \cdot \psi + \partial_t \phi$.

The Jacobian of the space-time projected inviscid flux $B : \mathbb{R}^m \times \mathbb{S}_d \rightarrow \mathbb{R}^{m \times m}$ is

$$B : (W, \eta) \mapsto \frac{\partial[\mathcal{F}(W)\eta]}{\partial W}. \quad (9)$$

Any $\eta \in \mathbb{S}_d$ can be written as $\eta = (n_x, n_t)$ where $n_x \in \mathbb{R}^d$ and $n_t \in \mathbb{R}$, and n_x can be expanded $n_x = \eta_x \|n_x\|$ with $\eta_x \in \mathbb{S}_{d'}$ (η_x is uniquely defined as $n_x/\|n_x\|$ in the case where $n_x \neq 0$, otherwise it is arbitrary). From

this expansion and the form of the inviscid flux in (8), the space-time Jacobian can be related to the original Jacobian

$$B(W, \eta) = B_x(W, \eta_x) \|n_x\| + n_t I_m. \quad (10)$$

The eigenvalue decomposition of the projected Jacobian is denoted

$$B(W, \eta) = V(W, \eta) \Lambda(W, \eta) V(W, \eta)^{-1}, \quad (11)$$

where $\Lambda : \mathbb{R}^m \times \mathbb{S}_d$ is a diagonal matrix containing the real eigenvalues of B and the columns of $V : \mathbb{R}^m \times \mathbb{S}_d \rightarrow \mathbb{R}^{m \times m}$ contain the corresponding right eigenvectors. Owing to the relationship between the projected Jacobians of the spatial and space-time inviscid fluxes (10), their eigenvalue decompositions are related as

$$\Lambda(W, \eta) = \Lambda_x(W, \eta_x) \|n_x\| + n_t I_m, \quad V(W, \eta) = V_x(W, \eta_x) \quad (12)$$

Linearized Riemann solvers for the space-time conservation law (7) and the associated numerical fluxes, $\mathcal{H} : \mathbb{R}^m \times \mathbb{R}^m \times \mathbb{S}_d \rightarrow \mathbb{R}^m$, are obtained from the formulas in Section 2.1 with the space-time quantities in place of the corresponding spatial terms

$$\mathcal{H} : (W^+, W^-, \eta) \mapsto \frac{1}{2} (\mathcal{F}(W^+) \eta + \mathcal{F}(W^-) \eta) + \frac{1}{2} \tilde{B}(W^+, W^-, \eta) (W^+ - W^-). \quad (13)$$

The Jacobian of the linearized Riemann problem $\tilde{B} : \mathbb{R}^m \times \mathbb{R}^m \times \mathbb{S}_d \rightarrow \mathbb{R}^{m \times m}$ is

$$\tilde{B}(W^+, W^-, \eta) = \left| B(\hat{U}(W^+, W^-), \eta) \right|, \quad (14)$$

which can be directly written in terms of spatial quantities using (12)

$$\tilde{B}(W^+, W^-, \eta) = V_x(\hat{W}, \eta_x) \left| \Lambda_x(\hat{W}, \eta_x) \|n_x\| + n_t I_m \right| V_x(\hat{W}, \eta_x)^{-1}, \quad (15)$$

where $\hat{W} = \hat{U}(W^+, W^-)$ was introduced for brevity.

Remark 4. *The space-time version of the Vijayasundaram flux uses a linear Riemann problem of the form (13) with the arithmetic average $\hat{U}(W^+, W^-) = (W^+ + W^-)/2$ and the flux average replaced with the linearized flux average $B(\hat{U}(W^+, W^-), \eta) \hat{U}(W^+, W^-)$ [52]. The space-time Rusanov flux takes the linearized Riemann problem matrix to be*

$$\tilde{B} : (W^+, W^-, \eta) \mapsto \max \{ \|\Lambda(W^+, \eta)\|_\infty, \|\Lambda(W^-, \eta)\|_\infty \} I_m, \quad (16)$$

which can be directly written in terms of spatial quantities using (12)

$$\tilde{B} : (W^+, W^-, \eta) \mapsto \max \{ \|\Lambda_x(W^+, \eta_x) \|n_x\| + n_t I_m\|_\infty, \|\Lambda_x(W^-, \eta_x) \|n_x\| + n_t I_m\|_\infty \} I_m. \quad (17)$$

Remark 5. *The space-time formulation of the conservation law (7) can be readily obtained from spatial formulation (1) with the physical flux and source term in (8) and popular numerical flux functions based on linearized Riemann solvers in (13)-(15). This allows for a general, systematic implementation of space-time conservation laws from the standard spatial formulation, which eliminates one of the implementation burdens associated with space-time methods.*

2.3. Transformed space-time conservation law on a fixed reference domain

Because the proposed numerical method is based on deforming the space-time domain to track discontinuities with the computational grid, it is convenient to recast the space-time conservation law such that domain deformations appear explicitly. To this end, we define $\bar{\Omega} \subset \mathbb{R}^d$ as a fixed space-time reference domain, which we require to take the form of a space-time slab, i.e., $\bar{\Omega} := \Omega_x \times \mathcal{T}$. Let \mathbb{G} be the collection of diffeomorphisms from the reference domain to the physical domain, i.e., for any $\mathcal{G} \in \mathbb{G}$, $\mathcal{G} : \bar{\Omega} \rightarrow \Omega$ with $\mathcal{G} : \bar{z} \mapsto \mathcal{G}(\bar{z})$, that preserve the space-time slab structure of the physical domain (slab-preserving mappings will be constructed in Section 3). The space-time conservation law in (7) can be reformulated as a conservation law over the

reference domain as [56]

$$\bar{\nabla} \cdot \bar{\mathcal{F}}(\bar{U}; G) = \bar{\mathcal{S}}(\bar{U}; g), \quad (18)$$

where $\bar{U} : \bar{\Omega} \rightarrow \mathbb{R}^m$ is the solution of the transformed conservation law, $\bar{\mathcal{F}} : \mathbb{R}^m \times \mathbb{R}^{d \times d} \rightarrow \mathbb{R}^{m \times d}$ and $\bar{\mathcal{S}} : \mathbb{R}^m \times \mathbb{R} \rightarrow \mathbb{R}^m$ are the transformed flux function and source term, respectively, $\bar{\nabla} \cdot$ is the divergence operator in the reference domain $\bar{\Omega}$ defined as $(\bar{\nabla} \cdot \psi)_i = \partial_{\bar{z}_j} \psi_{ij}$, and the deformation gradient $G : \bar{\Omega} \rightarrow \mathbb{R}^{d \times d}$ and mapping Jacobian $g : \bar{\Omega} \rightarrow \mathbb{R}$ are

$$G : \bar{z} \mapsto \partial_{\bar{z}} \mathcal{G}(\bar{z}), \quad g : \bar{z} \mapsto \det G(\bar{z}). \quad (19)$$

The reference domain quantities are defined in terms of the corresponding physical domain quantities as [56]

$$\bar{U}(\bar{z}) = U(\mathcal{G}(\bar{z})), \quad \bar{\mathcal{F}} : (\bar{W}; \Theta) \mapsto (\det \Theta) \mathcal{F}(\bar{W}) \Theta^{-T}, \quad \bar{\mathcal{S}} : (\bar{W}; q) \mapsto q \mathcal{S}(\bar{W}). \quad (20)$$

Transformed numerical flux functions, $\bar{\mathcal{H}} : \mathbb{R}^m \times \mathbb{R}^m \times \mathbb{S}_d \times \mathbb{R}^{d \times d} \mapsto \mathbb{R}^m$, by virtue of being a surrogate for the inviscid flux projected in a particular direction are related to the physical numerical flux [59] as

$$\bar{\mathcal{H}} : (\bar{W}^+, \bar{W}^-, \bar{\eta}; \Theta) \mapsto \sigma \mathcal{H}(\bar{W}^+, \bar{W}^-, \sigma^{-1}(\det \Theta) \Theta^{-T} \bar{\eta}) \quad (21)$$

where $\sigma = \|(\det \Theta) \Theta^{-T} \bar{\eta}\|$ is defined for brevity.

Remark 6. Analogous to Remark 5, the transformed conservation law (18) can readily be obtained from the space-time conservation (7) with the transformed flux and source term defined in (20) and the transformation of any numerical flux in (21). This allows for a general, systematic implementation of transformed space-time conservation laws from the standard spatial formulation.

2.4. Discontinuous Galerkin discretization of the transformed space-time conservation law

Because we are interested in high-order shock fitting solutions, we discretize the transformed conservation law (18) with a discontinuous Galerkin method [18] with high-order piecewise polynomials spaces used to approximate the state \bar{U} and domain mapping \mathcal{G} . To this end, let $\bar{\mathcal{E}}_h$ represent a discretization of the reference domain Ω_0 into non-overlapping, potentially curved, computational elements. To establish the finite-dimensional DG formulation, we introduce the DG approximation (trial) space of discontinuous piecewise polynomials associated with the mesh $\bar{\mathcal{E}}_h$

$$\mathcal{V}_h^p := \{v \in [L^2(\bar{\Omega})]^m \mid v|_{\bar{K}} \in [\mathcal{P}_p(\bar{K})]^m, \forall \bar{K} \in \bar{\mathcal{E}}_h\}, \quad (22)$$

where $\mathcal{P}_p(\bar{K})$ is the space of polynomial functions of degree at most $p \geq 0$ over the domain \bar{K} . Furthermore, we define the space of globally continuous piecewise polynomials of degree q associated with the mesh $\bar{\mathcal{E}}_h$ as

$$\mathcal{W}_h := \{v \in C^0(\bar{\Omega}) \mid v|_{\bar{K}} \in \mathcal{P}_q(\bar{K}), \forall \bar{K} \in \bar{\mathcal{E}}_h\} \quad (23)$$

and discretize the domain mapping with the corresponding vector-valued space $[\mathcal{W}_h]^d$. With these definitions, the DG variational problem is: given $\mathcal{G}_h \in [\mathcal{W}_h]^d$, find $\bar{U}_h \in \mathcal{V}_h^p$ such that for all $\bar{\psi}_h \in \mathcal{V}_h^{p'}$, we have

$$r_h^{p',p}(\bar{\psi}_h, \bar{U}_h; \bar{\nabla} \mathcal{G}_h) = 0 \quad (24)$$

where $p' \geq p$ and the global residual function $r_h^{p',p} : \mathcal{V}_h^{p'} \times \mathcal{V}_h^p \times [\mathcal{W}_h]^d \rightarrow \mathbb{R}$ is defined in terms of elemental residuals $r_K^{p',p} : \mathcal{V}_h^{p'} \times \mathcal{V}_h^p \times [\mathcal{W}_h]^d \rightarrow \mathbb{R}$ as

$$r_h^{p',p}(\bar{\psi}_h, \bar{W}_h; \Theta_h) \mapsto \sum_{\bar{K} \in \bar{\mathcal{E}}_h} r_{\bar{K}}^{p',p}(\bar{\psi}_h, \bar{W}_h; \Theta_h). \quad (25)$$

The elemental residuals come directly from a standard DG formulation applied to the transformed space-time conservation law in (18)

$$\begin{aligned}
r_{\bar{K}}^{p',p} : (\bar{\psi}_h, \bar{W}_h; \Theta_h) \mapsto & \int_{\partial \bar{K}} \bar{\psi}_h \cdot \bar{\mathcal{H}}(W_h^+, W_h^-, \bar{\eta}_h; \Theta_h) dS \\
& - \int_{\bar{K}} \bar{\mathcal{F}}(W_h; \Theta_h) : \bar{\nabla} \bar{\psi}_h dV \\
& - \int_{\bar{K}} \bar{\psi}_h \cdot \bar{\mathcal{S}}(W_h; \det \Theta_h) dV,
\end{aligned} \tag{26}$$

where $\bar{\eta}_h : \partial \bar{K} \mapsto \mathbb{R}^d$ is the outward unit normal to an element $\bar{K} \in \bar{\mathcal{E}}_h$, and \bar{W}_h^+ (\bar{W}_h^-) denotes the interior (exterior) trace of $\bar{W}_h \in \mathcal{V}_h^p$ to the element.

Finally, we introduce a basis for the test space ($\mathcal{V}_h^{p'}$), trial space (\mathcal{V}_h^p), and domain mapping space ($[\mathcal{W}_h]^d$) to reduce the weak formulation in (24)-(26) to a system of nonlinear algebraic equations. In the case where $p = p'$, we have

$$\mathbf{r} : \mathbb{R}^{N_u} \times \mathbb{R}^{N_x} \rightarrow \mathbb{R}^{N_u}, \quad \mathbf{r} : (\mathbf{u}, \mathbf{x}) \mapsto \mathbf{r}(\mathbf{u}, \mathbf{x}), \tag{27}$$

where $N_u = \dim(\mathcal{V}_h^p)$ and $N_x = \dim([\mathcal{W}_h]^d)$, which is the residual of a standard space-time DG method. Furthermore, we define the algebraic enriched residual associated with a test space of degree $p' > p$ ($p' = p + 1$ in this work) as

$$\mathbf{R} : \mathbb{R}^{N_u} \times \mathbb{R}^{N_x} \rightarrow \mathbb{R}^{N'_u}, \quad \mathbf{R} : (\mathbf{u}, \mathbf{x}) \mapsto \mathbf{R}(\mathbf{u}, \mathbf{x}), \tag{28}$$

where $N'_u = \dim(\mathcal{V}_h^{p'})$, which will be used to construct the implicit shock tracking objective function. Finally, to maintain a connection between the algebraic and functional representation of the DG solution, we define the operator $\Xi : \mathbb{R}^{N_u} \rightarrow \mathcal{V}_h^p$ that maps $\mathbf{v} \in \mathbb{R}^{N_u}$ to its representation as a function over the reference domain $\bar{\Omega}$, $V_h = \Xi(\mathbf{v}) \in \mathcal{V}_h^p$.

3. Mesh generation of space-time slab

In this section, we address construction of a conforming, simplex-only mesh $\bar{\mathcal{E}}_h$ of the space-time slab. We insist on a simplex-only mesh because element removal via edge collapse is well-defined in any dimension and key to robust shock tracking [20]. Furthermore, we construct a conforming mesh because it makes construction of the continuous space $[\mathcal{W}_h]^d$ simple and convenient using standard finite elements where adjacent elements share nodes. Non-conforming meshes can be used provided constraints are added to ensure the mapped mesh remains valid (no gaps or overlaps).

One option to construct a conforming, simplex-only mesh of the space-time slab $\bar{\Omega}$ is to directly use an unstructured mesh generator in the $(d' + 1)$ -dimensional domain. While substantial progress has been made in higher dimensional mesh generation [5, 55, 51, 1], direct and automatic generation of high-order, high-quality (sliver-free) meshes in dimensions beyond $d = d' + 1 = 2$ remains a challenge. Automation is particularly important to avoid user intervention as a simulation advances in time (between slabs). Furthermore, this approach may neglect important information from the previous time slab, e.g., the location of tracked discontinuities in the present setting. Instead, we utilize an extrusion approach [24, 53, 12] whereby the (simplicial) elements of a mesh of the spatial domain are extruded into the temporal dimension to define space-time prismatic elements, which are subsequently split into space-time simplices. With this approach, only a complete mesh of the spatial domain is required along with two simple mesh operations: extrusion of a d' -dimensional simplex and splitting of a $(d' + 1)$ -dimensional prism into simplices. We detail these steps individually in the remainder of this section, including an approach to split high-order elements.

3.1. Construction of d' -dimensional (spatial) simplicial mesh

In the general case where multiple slabs are used to cover the temporal domain of interest, we distinguish two cases. For the first time slab, a (potentially) curved simplex-only mesh, $\bar{\mathcal{E}}_{x,h}$, of the spatial domain Ω_x is constructed using standard mesh generation approaches. While this can suffer from the issues discussed in the previous section, it only needs to be performed once for an entire time-dependent simulation (as opposed to being required for each slab) and is a standard part of computational physics workflows. For all other

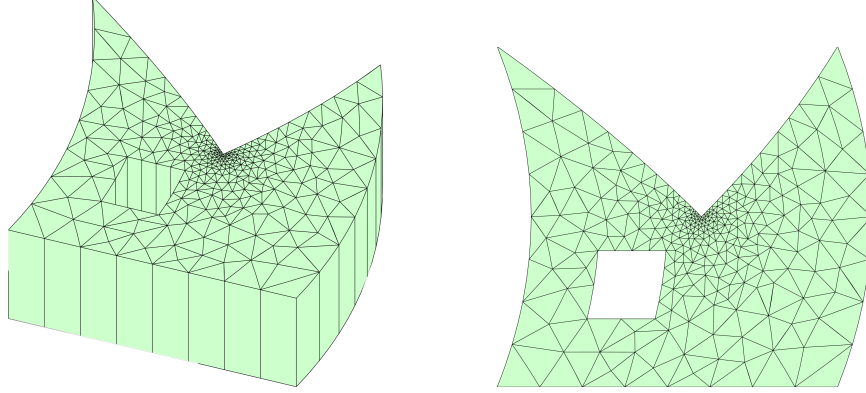


Figure 1: Space-time mesh in $d' + 1 = 3$ (left) and $d' = 2$ spatial mesh extracted from top of time slab (right).

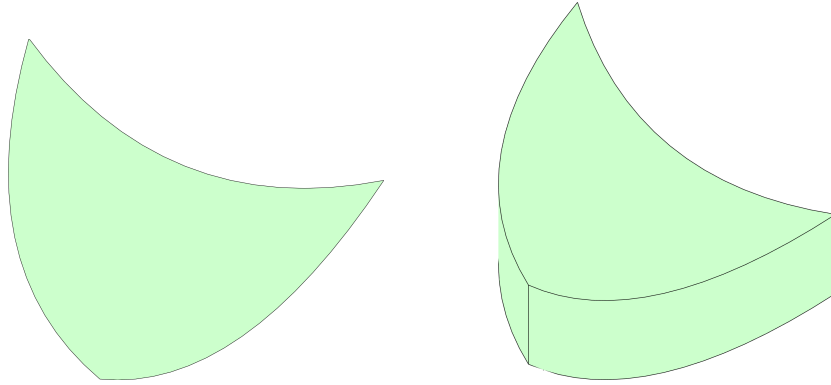


Figure 2: Curved triangle in $d' = 2$ spatial domain (left) extruded to triangular prism in $d' + 1 = 3$ space-time domain (right).

time slabs, the spatial mesh is extracted from the top boundary $\partial\Omega_x \times \{t_1\}$ of the space-time mesh of the previous time slab (Figure 1). This approach ensures the spatial mesh $\bar{\mathcal{E}}_{x,h}$ contains all of the features (e.g., refinement regions, tracked discontinuities, element curvature) present in the mesh of the previous space-time slab.

3.2. Extrusion of d' -dimensional (spatial) simplicial mesh

Once a simplex-only mesh $\bar{\mathcal{E}}_{x,h}$ of the spatial domain Ω_x is available, each spatial element is extruded in the temporal dimension to form a space-time simplicial prism. That is, the mesh $\bar{\mathcal{E}}_h$ of the space-time slab $\bar{\Omega} = \Omega_x \times \mathcal{T}$ is defined as

$$\bar{\mathcal{E}}_h = \bigcup_{K_x \in \bar{\mathcal{E}}_{x,h}} K_x \times \mathcal{T}, \quad (29)$$

where $K_x \times \mathcal{T} \subset \bar{\Omega}$ is a (potentially) curved simplicial prism in d -dimensions (Figure 2). This extrusion approach preserves characteristics of the spatial mesh throughout the space-time slab such as refinement regions and tracked discontinuities.

3.3. High-order space-time mesh refinement via transformations

The final step required to create a mesh of a space-time slab is to split the potentially curved simplicial prism into simplices. We define a systematic procedure that splits a straight-sided version of the elements in the parent domain and uses the isoparametric mapping to define a high-order splitting in the reference domain. Then the domain mapping \mathcal{G} defines a high-order splitting in the physical domain. This is simpler than refining potentially curved elements in the reference domain. This approach will be used to both split prism elements into simplices, as well as subdivide simplex elements into smaller simplicies (for mesh refinement, Section 4.5) while still maintaining potentially curved high-order elements.

To this end, we define a parent domain $\Omega_\square \subset \mathbb{R}^d$ along with a transformation $\mathcal{Y}_{\bar{K}} : \Omega_\square \rightarrow \bar{K}$, $\mathcal{Y}_{\bar{K}} : \xi \mapsto \mathcal{Y}_{\bar{K}}(\xi)$ that maps Ω_\square to the element $\bar{K} \in \bar{\mathcal{E}}_h$. In this work, the parent domain Ω_\square will either be the unit simplex $\mathcal{K}_0^d \subset \mathbb{R}^d$ or simplicial prism \mathcal{SP}_0^d , defined as

$$\begin{aligned} \mathcal{K}_0^d &:= \left\{ \xi \in \mathbb{R}^d \mid \sum_{i=1}^d \xi_i \leq 1, \xi_j \geq 0, j = 1, \dots, d \right\} \\ \mathcal{SP}_0^d &:= \left\{ \xi \in \mathbb{R}^d \mid \sum_{i=1}^{d-1} \xi_i \leq 1, \xi_j \geq 0, j = 1, \dots, d-1, -1 \leq \xi_d \leq 1 \right\}, \end{aligned} \quad (30)$$

and $\mathcal{Y}_{\bar{K}} \in [\mathcal{P}_q(\Omega_\square)]^d$ is defined using a standard isoparametric approach

$$\mathcal{Y}_{\bar{K}} : \xi \mapsto \sum_{I=1}^n \bar{z}_I^{\bar{K}} \varphi_I(\xi), \quad (31)$$

where $\{\bar{z}_I^{\bar{K}}\}_{I=1}^n \subset \mathbb{R}^d$ are the nodal coordinates of the high-order element $\bar{K} \in \bar{\mathcal{E}}_h$ in the reference domain, $\{\varphi_I\}_{I=1}^n$ is a Lagrangian basis of $\mathcal{P}_q(\Omega_\square)$, and $n = \dim \mathcal{P}_q(\Omega_\square)$. Composition of the isoparametric mapping $\mathcal{Y}_{\bar{K}}$ with the domain mapping \mathcal{G} maps the parent element Ω_\square to the physical domain. This setup is illustrated in Figure 3.

Remark 7. For brevity, we use isoparametric mapping to refer to the mapping from parent domain (Ω_\square) to reference domain element (\bar{K}), regardless of the relationship between p (solution polynomial degree) and q (domain polynomial degree).

Next, let $\Pi \in 2^{\Omega_\square}$ define a decomposition of the parent element into subdomains such that $\bigcup_{Z \in \Pi} Z = \Omega_\square$ and $Z \cap Z' = \emptyset$ for $Z, Z' \in \Pi$ with $Z \neq Z'$, and let $\bar{\mathcal{E}}_h^r \subset \bar{\mathcal{E}}_h$ denote the subset of elements to be partitioned. Then a new mesh $\bar{\mathcal{E}}_h^r$ of $\bar{\Omega}$ is obtained from the original mesh $\bar{\mathcal{E}}_h$ by composing the isoparametric mapping for each element in $\bar{\mathcal{E}}_h^r$ with the refinement operator

$$\bar{\mathcal{E}}_h' = \{\mathcal{Y}_{\bar{K}}(Z) \mid \bar{K} \in \bar{\mathcal{E}}_h^r, Z \in \Pi\} \cup (\bar{\mathcal{E}}_h \setminus \bar{\mathcal{E}}_h^r). \quad (32)$$

Furthermore, by mapping each element of this new mesh $\bar{\mathcal{E}}_h'$, a mesh of the physical domain Ω is defined as

$$\mathcal{E}_h' = \{\mathcal{G}(\bar{K}') \mid \bar{K}' \in \bar{\mathcal{E}}_h'\}. \quad (33)$$

This process is illustrated in Figure 3.

If the original mesh $\bar{\mathcal{E}}_h$ is the simplicial prism mesh produced in Section 3.2, $\bar{\mathcal{E}}_h^r = \bar{\mathcal{E}}_h$, and Π is an operator that decomposes \mathcal{SP}_0^d into simplices (Section 3.3.1), the resulting mesh $\bar{\mathcal{E}}_h'$ will be a simplex-only mesh of $\bar{\Omega}$. On the other hand, if $\bar{\mathcal{E}}_h$ is a simplex-only mesh of $\bar{\Omega}$ and Π is an operator that decomposes \mathcal{K}_0^d into smaller simplices, the resulting mesh $\bar{\mathcal{E}}_h'$ will be a refined simplex-only mesh of $\bar{\Omega}$. However, in both of these cases, $\bar{\mathcal{E}}_h'$ is not guaranteed to be conforming even if $\bar{\mathcal{E}}_h$ is a conforming mesh. In the remainder of this section, we discuss strategies to ensure the new mesh $\bar{\mathcal{E}}_h'$ is conforming, which will in turn guarantee the physical mesh \mathcal{E}_h' is conforming because the mappings $\mathcal{G} \in [\mathcal{W}_h]^d$ are continuous.

Remark 8. The expression for the refined mesh in (32) is a simplified version of the algorithm used in practice because it only uses a single parent element decomposition Π . We usually introduce several Ω_\square decompositions, which are used selectively to ensure a conforming mesh is produced. This can be written as

$$\bar{\mathcal{E}}_h' = \{\mathcal{Y}_{\bar{K}}(Z) \mid \bar{K} \in \bar{\mathcal{E}}_h^r, Z \in \Pi_{\bar{K}}\} \cup (\bar{\mathcal{E}}_h \setminus \bar{\mathcal{E}}_h^r), \quad (34)$$

where $\Pi_{\bar{K}} \in 2^{\Omega_\square}$ is the decomposition used for element $\bar{K} \in \bar{\mathcal{E}}_h$. Details on construction of conforming refinements are included in Sections 3.3.1-3.3.2.

3.3.1. Prism-to-simplex refinement

In the $d = 2$ case, a simplicial prism is simply a quadrilateral, which can be split with one or both diagonal lines (Figure 4). Any of these splittings can be applied to any subset of elements of the simplicial

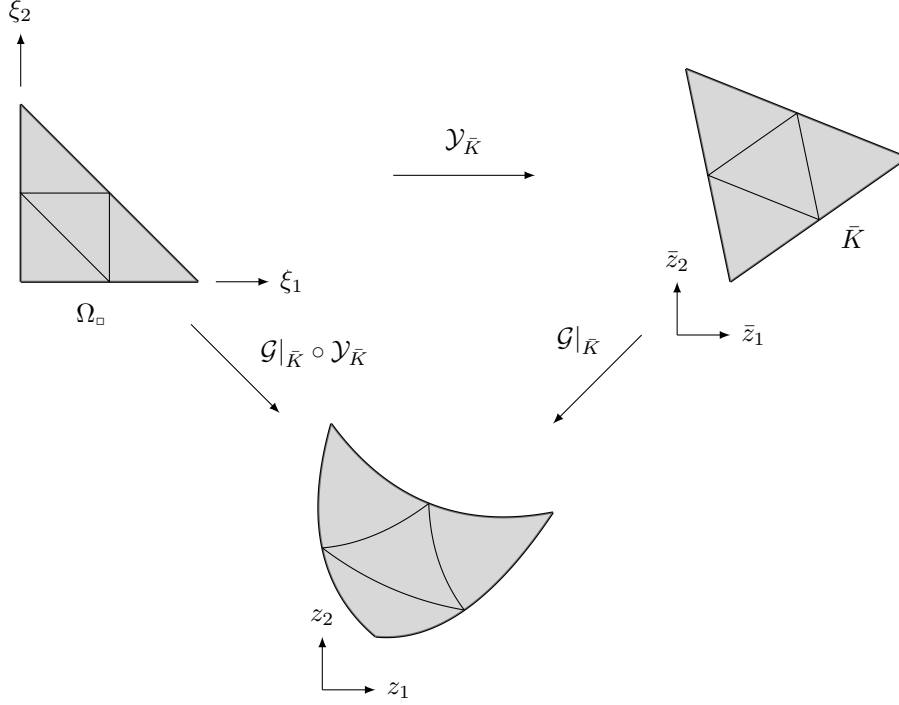


Figure 3: Schematic of high-order element refinement whereby the refinement operator Π is applied to the parent element, which is mapped via the isoparametric mapping of the unrefinement element $\mathcal{Y}_{\bar{K}}$ to define a refinement in the reference domain $\bar{\Omega}$, which is in turn mapped via the transformation \mathcal{G} to define a refinement in the physical domain Ω .

mesh, regardless of element orientation, and the resulting simplicial mesh is guaranteed to be conforming.

In the $d > 3$ case, \mathcal{SP}_0^d contains $d + 2$ faces: two simplex “caps“ and d simplicial prism “sides”. We aim to define a decomposition (Π) of \mathcal{SP}_0^d such that if it is applied to all elements of the prismatic mesh via (32), the resulting simplex-only mesh is guaranteed to be conforming without requiring global mesh operations. This is accomplished by decomposing \mathcal{SP}_0^d in such a way that the decomposition of its $d + 2$ faces into $(d - 1)$ -dimensional simplices is independent of the orientation of the element. Any decomposition of \mathcal{SP}_0^d that guarantees such a decomposition of its faces will trivially lead to a conforming simplex-only mesh. A dimension-independent approach based on this concept first applies an orientation-independent decomposition to partition each face into $(d - 1)$ -dimensional simplices. Then the vertices of each $(d - 1)$ -dimensional simplex are connected to a central node in the d -dimensional prism to form d -dimensional simplicies. Assuming the simplicial caps are not refined, this procedure splits \mathcal{SP}_0^d into N_d simplicies, where

$$N_d = dN_{d-1} + 2 \quad (35)$$

for $d > 2$ and $N_2 = 4$, which leads to $N_3 = 14$ and $N_4 = 58$ ($d = 3$ case in Figure 5). Alternatively, a constrained Delaunay triangulation can be used to form $N_3 = 11$ d -dimensional simplicies without introducing a central node. While these approaches are general and allow each element to be split independently of its neighbors, it produces large meshes in $d > 2$.

Remark 9. *In this work, we use the approach that splits the simplicial prism into $N_2 = 4$ and $N_3 = 14$ simplicies instead of the more efficient approaches, i.e., split with a single diagonal in $d = 2$ ($N_2 = 2$) and split without a central node in $d = 3$ ($N_3 = 11$). Despite the creation of more simplicies, we have observed the chosen approach improves the robustness of shock fitting. This is attributed to the fact that the chosen splitting is essentially uniform refinement and, as such, regardless of the trajectory of discontinuities, there will be a face that provides a reasonable initial guess to its space-time trajectory. This could also be achieved with a shock-dependent splitting, which was not pursued in this work.*

Remark 10. *In the $d = 3$ case, there are several ways to split \mathcal{SP}_0^d into $N_3 = 4$ simplicies although each*

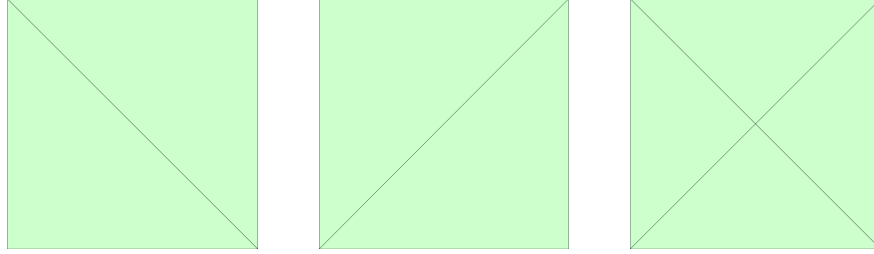


Figure 4: Conforming decompositions ($d = 2$) of a quadrilateral into triangles using a single diagonal (*left, center*), and both diagonals (*right*).

element cannot be split independently. Rather, each prism must be split into four simplices based on the partition of the neighbors to ensure the diagonals of each face conform, which requires global mesh operations [53].

3.3.2. Simplex-to-simplex refinement

We consider two approaches to refine a simplex into smaller simplices (Π), which will be used for adaptive mesh refinement in Section 4.5. A general, dimension-independent approach is known as an edge split [34, 28], whereby a new node is introduced at the midpoint of one edge of the original simplex and the unique plane that passes through this point and the $d - 1$ vertices of the simplex not associated with the original edge is used to split the simplex into two smaller simplices (Figure 6). To ensure a conforming mesh, all simplices that share the edge being split must also be split using the general form of the mesh refinement in (34). Another approach that is only practical in $d = 2$ is to split a triangle uniformly into four smaller triangles (Figure 6). To ensure the resulting mesh is conforming, all neighbors of an element that is uniformly refined must also be uniformly refined or the edge must be split [2, 30].

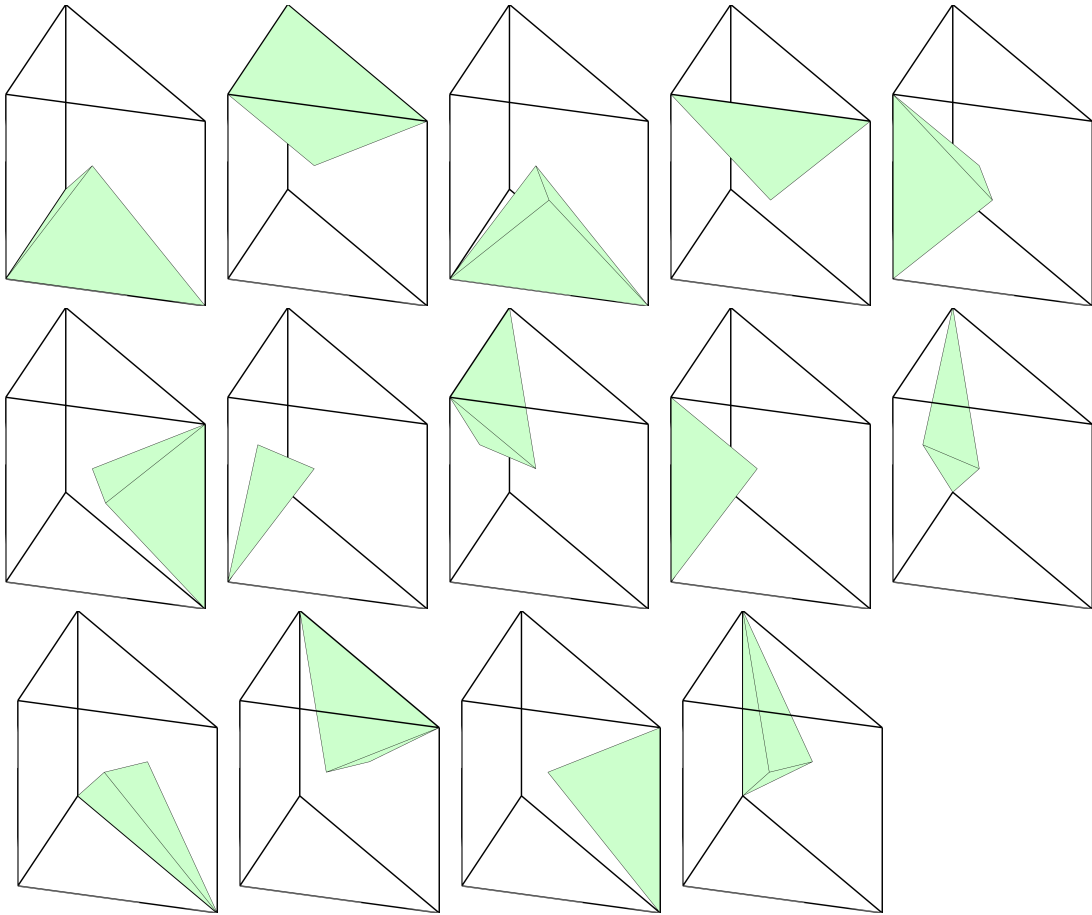


Figure 5: Conforming decomposition ($d = 3$) of a triangular prism into $N_3 = 14$ tetrahedra using a $d = 2$ conforming splitting of the quadrilateral faces and connecting all face/edge nodes to a central node.

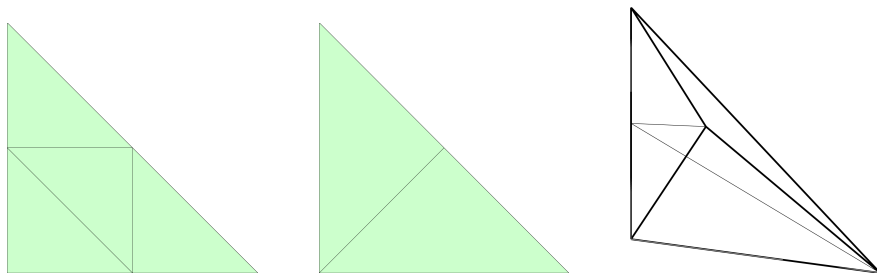


Figure 6: Conforming refinement of a simplices using uniform refinement in $d = 2$ (*left*), edge splitting in $d = 2$ (*center*), and edge splitting in $d = 3$ (*right*).

4. High-order implicit shock tracking over space-time slabs

In this section, we extend the HOIST method [59, 20] to the slab-based space-time setting with special attention given to the challenges and opportunities inherent in this setting. In particular, we construct admissible domain mappings over space-time slabs (Section 4.1), formulate the space-time HOIST method (Section 4.2), and discuss solution transfer between space-time slabs (Section 4.3). Additionally, we describe an approach to scale time slabs in the temporal direction (Section 4.4) such that well-conditioned space-time grids can be obtained, even when the solution contains waves with extreme speeds. Finally, we describe a simple approach to incorporate adaptive mesh refinement into the shock tracking solver (Section 4.5), describe an opportunity for efficiency that applies boundary conditions directly to shocks (Section 4.6) and summarize the complete algorithm (Section 4.7).

4.1. Admissible domain mappings

Following the approach in [20], we introduce a parametrization of the physical nodes

$$\phi : \mathbb{R}^{N_y} \rightarrow \mathbb{R}^{N_x}, \quad \phi : \mathbf{y} \mapsto \phi(\mathbf{y}), \quad (36)$$

where $\mathbf{y} \in \mathbb{R}^{N_y}$ are unconstrained degrees of freedom (DoFs), which guarantees the boundaries of the space-time slab are preserved. Using this parametrization, the unconstrained DoFs can be moved freely without modifying the computational domain, which simplifies the central optimization problem in the next section because boundary-preserving constraints are unnecessary. Approaches to construct the parametrization ϕ for straight-sided [20] and curved [57] boundaries are detailed in previous work.

In time-dependent problems, discontinuities can interact with the spatial boundaries, e.g., leave the domain or reflect off a wall, at unknown times. If such an event occurs near, but not at, the top of a time slab, there will likely be insufficient resolution in the mesh to track it. To avoid this issue, we follow the approach proposed in [11] to allow the top of the time slab to translate so the shock-boundary interaction can be tracked (Figure 7). Mathematically, we let $\mathcal{I}_t \subset \{1, \dots, N_x\}$ be the temporal mesh DoFs associated with the nodes on the top of the time slab. Then the unconstrained DoFs are written as $\mathbf{y} = (\mathbf{y}', \zeta)$ and the parametrization satisfies

$$\phi_i(\mathbf{y}) = \zeta, \quad i \in \mathcal{I}_t \quad (37)$$

where $\mathbf{y}' \in \mathbb{R}^{N_y-1}$ are the unconstrained DoFs associated with the mesh degrees of freedom away from \mathcal{I}_t and $\zeta \in \mathbb{R}$ is the translation of the top of the time slab. Unlike the parametrization in [20], this parametrization allows the space-time slab to change; however, it guarantees the slab structure is preserved (because the top boundary translates in the temporal direction). By incorporating the translating boundary into the admissible domain mapping, we are relying on the shock tracking method to position it appropriately. More general parametrizations of the upper temporal boundary of a space-time slab can be considered to break the slab structure for problems with events (e.g., shock-shock or shock-boundary interactions) that occur at similar, but not the same, time (Section 5.3.1).

4.2. Optimization formulation

The HOIST method introduced in [56, 59] simultaneously computes the discrete solution of the conservation law and the nodal coordinates of the mesh that cause element faces to align with discontinuities. This is achieved through a fully discrete, full space PDE-constrained optimization formulation with the optimization variables taken to be the discrete flow solution and unconstrained mesh DoFs over the time slab

$$(\mathbf{u}^*, \mathbf{y}^*) := \arg \min_{\mathbf{u} \in \mathbb{R}^{N_u}, \mathbf{y} \in \mathbb{R}^{N_y}} f(\mathbf{u}, \mathbf{y}) \quad \text{such that} \quad \mathbf{r}(\mathbf{u}, \phi(\mathbf{y})) = \mathbf{0}, \quad (38)$$

where $f : \mathbb{R}^{N_u} \times \mathbb{R}^{N_y} \rightarrow \mathbb{R}$ is the objective function and $\mathbf{x}^* = \phi(\mathbf{y}^*)$ are the physical nodes of the shock-aligned space-time slab mesh with associated flow solution \mathbf{u}^* . The objective function is composed of two terms as

$$f : (\mathbf{u}, \mathbf{y}) \mapsto f_{\text{err}}(\mathbf{u}, \mathbf{y}) + \kappa^2 f_{\text{msh}}(\mathbf{y}_s) \quad (39)$$

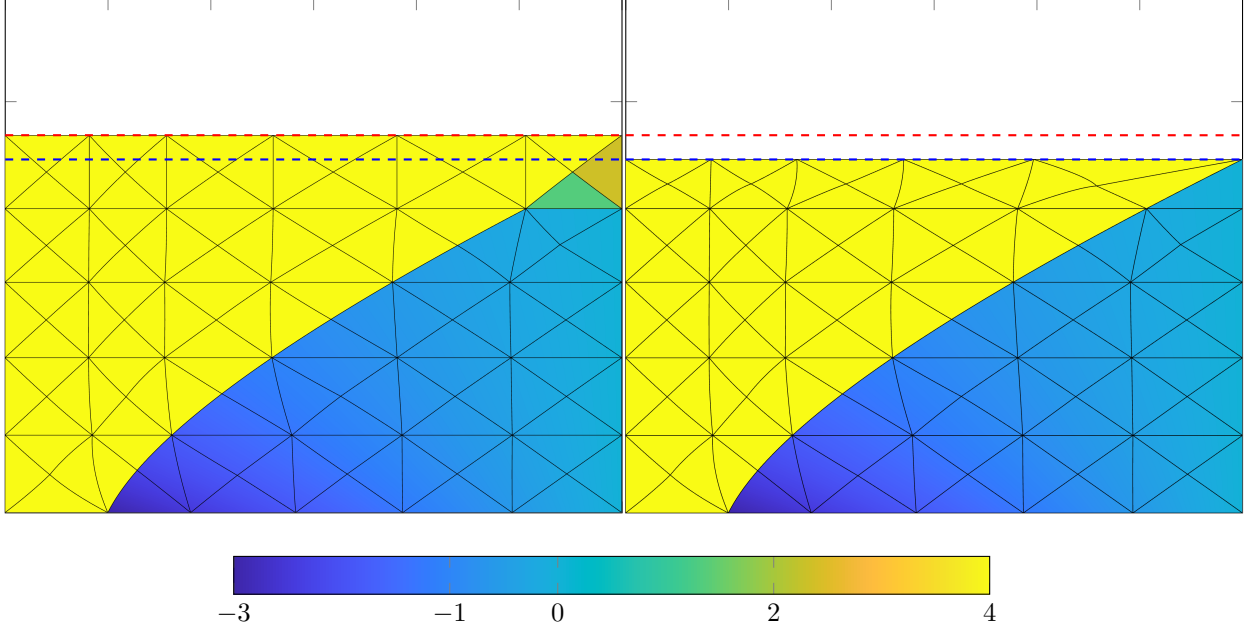


Figure 7: Demonstration of translating upper boundary of space-time slab. With *a priori* slab heights, there may be insufficient resolution in the mesh to track shock-boundary interactions (*left*), whereas a translating upper boundary allows the slab height to be determined by the shock tracking framework such that the shock-boundary interaction is tracked (*right*). Legend: *a priori* choice of time slab height (---), location of shock-boundary interaction (---).

which balances alignment of the mesh with non-smooth features and the quality of the elements, $f_{\text{err}} : \mathbb{R}^{N_u} \times \mathbb{R}^{N_y} \rightarrow \mathbb{R}$ is the alignment term taken as the norm of the enriched residual

$$f_{\text{err}} : (\mathbf{u}, \mathbf{y}) \mapsto \frac{1}{2} \|\mathbf{R}(\mathbf{u}, \phi(\mathbf{y}))\|_2^2, \quad (40)$$

f_{msh} is a mesh distortion term defined in [59], and $\kappa \in \mathbb{R}_{>0}$ is a mesh quality parameter. The mesh distortion term is designed to blow up if the Jacobian of the mapping goes to zero, which ensures the domain mapping will never become singular. The HOIST optimization formulation in (38) is identical to the HOIST formulation in [59, 20] over a space-time slab. As such, we use the sequential quadratic programming (SQP) solver described in [59, 20] to solve (38).

Remark 11. *In addition to avoiding global temporal coupling, space-time slabs also reduce the difficulty of the shock tracking problem (38), especially for problems with complex interactions that evolve over time. This is a result of shock tracking only being performed over a (potentially) small portion of the domain, which limits the temporal complexity.*

4.3. Boundary conditions and inter-slab solution transfer

Boundary conditions at the bottom of the first slab $\Omega_x \times \{t_0\}$ as well as on the spatial boundaries $\partial\Omega_x \times \mathcal{T}$ are specified as part of the problem description. Due to causality, boundary conditions at the top of any slab $\Omega_x \times \{t_1\}$ are extrapolated from the interior of the space-time domain. Finally, the boundary condition at the bottom of all slabs except the first must be interpolated from the top of the previous time slab. In practice, this involved interpolating the solution in the previous time slab at the quadrature nodes along the bottom boundary of the current slab. To ensure this interpolation does not need to be updated at every shock tracking iteration (or linearized for use in the SQP solver), the mapping in Section 4.1 is modified such that the domain deformation is the identity map when restricted to the bottom boundary. In practice, this is constructed by fixing the domain parametrization to the reference mesh node along the bottom boundary. This does not interfere with shock tracking at the bottom of the slab because any discontinuities that intersect the bottom of the slab would have been tracked by the previous slab, which would be preserved in the current slab through the extraction-based mesh generation (Section 3).

4.4. Nondimensionalization and scaling of space-time slab

There can be orders of magnitude difference between the spatial and temporal scales, depending on the problem and unit system used. This can lead to space-time meshes with excessive resolution in either the spatial or temporal dimension or highly skewed meshes (Figure 8). To circumvent this issue, we nondimensionalize the time-dependent conservation law with two goals: 1) ensure the components of the solution vector have similar magnitudes and 2) ensure the spatial dimensions and the temporal interval have similar magnitudes. The first is standard practice in CFD to improve the conditioning of the Jacobian of the DG residual (\mathbf{r}) and the latter is used to ensure well-conditioned space-time meshes are produced.

Let $D_x^* \in \mathbb{R}^{d' \times d'}$ be a diagonal matrix defining a spatial length scale in each dimension that maps a nondimensional domain $\hat{\Omega}_x$ to the dimensional domain Ω_x as $\hat{x} \mapsto x = D_x^* \hat{x}$. Furthermore, let $t^* \in \mathbb{R}$ be a temporal length scale that maps a nondimensional time \hat{t} to the dimensional time as $\hat{t} \mapsto t = t^* \hat{t}$ and $C \in \mathbb{R}^{m \times m}$ be a diagonal matrix containing the dimensionalization factor for each solution component (derived in part from the spatial and temporal length scales), which maps a nondimensional state vector to the dimensional one as $\hat{W}_x \mapsto W_x = C \hat{W}_x$. With these definitions, the conservation law in (1) can be written as a nondimensional conservation law over the nondimensional domain $\hat{\Omega}_x$ as

$$\frac{\partial \hat{U}_x}{\partial \hat{t}} + \hat{\nabla}_x \cdot \hat{\mathcal{F}}_x(\hat{U}_x) = \mathcal{S}_x(\hat{U}_x), \quad (41)$$

where $\hat{U}_x : \hat{\Omega}_x \rightarrow \mathbb{R}^m$ is the nondimensional conservative vector implicitly defined as the solution of (41) and related to the solution of the original conservation law as $\hat{U}_x(\hat{x}, \hat{t}) = C^{-1} U_x(D_x^* \hat{x}, t^* \hat{t})$, $\hat{\mathcal{F}}_x : \mathbb{R}^m \rightarrow \mathbb{R}^{m \times d}$ and $\hat{\mathcal{S}}_x : \mathbb{R}^m \rightarrow \mathbb{R}^m$ are the nondimensional flux function and source term, respectively, and related to the original terms as

$$\hat{\mathcal{F}}_x : \hat{W}_x \mapsto t^* C^{-1} \mathcal{F}_x(C \hat{W}_x) (D_x^*)^{-1}, \quad \hat{\mathcal{S}}_x : \hat{W}_x \mapsto t^* C^{-1} \mathcal{S}_x(C \hat{W}_x), \quad (42)$$

and $(\hat{\nabla}_x \cdot)$ is the nondimensional divergence operator. The procedure to formulate transformed space-time conservation laws in Sections 2.2-2.3 proceeds without modification with the spatial conservation law in (41) in place of the conservation law in (1).

In this work, we take the spatial scaling to be the identity matrix (with appropriate units for nondimensionalization) and focus on the choice of temporal scaling that leads to well-conditioned space-time simplices. In the case where the temporal dimension of the slab is much smaller than the spatial dimensions—usually occurring with fast moving waves evolving over small time scales—we take $t^* < 1$ to expand the temporal domain, effectively slowing the features. Otherwise, we take $t^* > 1$, which compresses the temporal domain, effectively speeding up the features and increasing the temporal resolution of the mesh. In both situations, the conditioning of the space-time simplices improves substantially (Figure 8). Once the characteristic length (D_x^*) and time (t^*) scales are determined, the solution scaling C usually follows directly from a characteristic mass scale.

4.5. Adaptive mesh refinement

In time-dependent problems, the solutions can develop complex features in localized regions of space-time, e.g., shock formation or features with small length scales, which calls for increased resolution using either h -, p -, or hp -refinement. In this work, we use the approach described in Sections 3.3 and 3.3.2 to h -refine elements in the refinement set $\bar{\mathcal{E}}_h^r$. The refinement set is the collection of elements where the magnitude of the enriched DG residual \mathbf{R} and the Persson-Peraire shock sensor [35, 36], $s_{\bar{K}} : \mathcal{V}_h^p \rightarrow \mathbb{R}$, $\bar{K} \in \bar{\mathcal{E}}_h$, is largest. The Persson-Peraire shock sensor, which identifies elements with oscillatory solutions, is defined as

$$s_{\bar{K}} : \bar{W}_h \mapsto \log_{10} \left(\sqrt{\frac{\int_{\bar{K}} (\chi(\bar{W}_h) - \mathcal{X}(\Pi_{p-1} \bar{W}_h))^2 dV}{\int_{\bar{K}} \chi(\bar{W}_h)^2 dV}} \right), \quad (43)$$

where $\Pi_{p-1} : \mathcal{V}_h^p \rightarrow \mathcal{V}_h^{p-1}$ is a projection onto the space of piecewise polynomials of total degree $p-1$ and $\chi : \mathbb{R}^m \rightarrow \mathbb{R}$ is a suitable scalar of the state. In this work we choose $\chi : (W_1, \dots, W_m) \mapsto W_1$ and define the refinement set as

$$\bar{\mathcal{E}}_h^r : (\mathbf{u}, \mathbf{x}) \mapsto \{\bar{K} \in \bar{\mathcal{E}}_h \mid \|\mathbf{R}_{\bar{K}}(\mathbf{u}, \mathbf{x})\| \geq c_1 R_{\max}(\mathbf{u}, \mathbf{x}) \text{ or } s_{\bar{K}}(\Xi(\mathbf{u})) \geq c_2 s_{\max}(\mathbf{u})\} \quad (44)$$

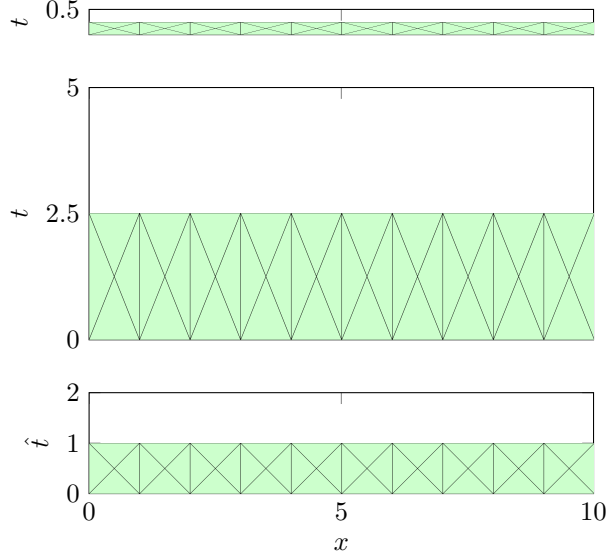


Figure 8: Schematic of a spatial domain $\Omega_x = (0, 10)$ and temporal domain corresponding to fast waves $\mathcal{T} = (0, 0.5)$ (*top*) and slower waves (or long-time dynamics) $\mathcal{T} = (0, 5)$ (*middle*) discretized using 10 elements in the spatial direction and 2 temporal slabs. The small temporal dimension compared to the spatial dimension leads to unnecessary refinement and poor quality elements (*top*), whereas the larger temporal domain leads to skewed/stretched elements (*middle*). Both can be fixed via nondimensionalization with $t^* < 1$ (transforms *top* to *bottom*) and $t^* > 1$ (transforms *middle* to *bottom*).

where

$$R_{\max} : (\mathbf{u}, \mathbf{x}) \mapsto \max_{\bar{K} \in \mathcal{E}_h} \|\mathbf{R}_{\bar{K}}(\mathbf{u}, \mathbf{x})\|, \quad s_{\max} : \mathbf{u} \mapsto \max_{\bar{K} \in \mathcal{E}_h} s_{\bar{K}}(\Xi(\mathbf{u})) \quad (45)$$

are the largest elemental residual norm and sensor, respectively, and $c_1, c_2 \in \mathbb{R}_{\geq 0}$ are indicator fractions whose default values are set to be $c_1 = 0.01$ and $c_2 = 0.01$ unless otherwise specified. We interrupt the HOIST solver at iteration k to refine the mesh, provided the number of elements in the mesh has not exceeded a user-defined limit, where k is any HOIST iteration with the DG residual below a user-defined threshold.

4.6. Shock boundary conditions

As detailed in [19], shock tracking provides an opportunity to reduce elements in the mesh that is not available to shock capturing methods. In situations where a discontinuity completely separates a region in which the flow is *known* from the downstream region, all elements in the region where the flow is known can be removed and the known flow used as an essential boundary condition applied directly to the shock surface. Such a strategy is available even if the shock position is not known by defining the mesh parametrization ϕ to allow arbitrary deformations to the shock-boundary and using the implicit shock tracking framework to determine its precise location. In the space-time setting, this approach can only be leveraged if a space-time discontinuity separates a region of space-time where the flow is known from the remainder of the space-time domain. This is applied by creating a spatial mesh of only the region where the flow is unknown at the initial condition, extruding it to form a space-time slab, applying a boundary condition that sets the flow solution to the known value on the elements that separate the regions where the flow is unknown vs. known, and using implicit shock tracking to position the shock-boundary appropriately. This technique is demonstrated for the accelerating shock problem (Section 5.1.1) and Shu-Osher problem (Section 5.3.2).

4.7. Summary

The complete slab-based space-time HOIST method for shock-dominated unsteady conservation laws is summarized in Algorithm 1.

Algorithm 1 Slab-based space-time HOIST method

Input: Reference spatial mesh $\bar{\mathcal{E}}_{x,h}$, desired time duration τ , nominal temporal slab height Δt

Output: Shock-aligned meshes and corresponding DG solution

- 1: $t = 0$
 - 2: **while** $t \leq \tau$ **do**
 - 3: **Construct mesh of space-time slab:** Extrude $\bar{\mathcal{E}}_{x,h}$ over time interval $(t, t + \Delta t)$ (Section 3.2) and split into simplices to form mesh of space-time slab \mathcal{E}'_h (Section 3.3)
 - 4: **Construct parametrization of space-time slab:** Define ϕ according to [20] with self-adjusting upper boundary (Section 4.1) and fixed lower boundary (Section 4.3) if $t > 0$
 - 5: **Solution initialization:** Initialize SQP iteration with the unconstrained DoFs of the reference mesh and the DG($p = 0$) solution on the reference mesh [20]
 - 6: **Implicit shock tracking on space-time slab:** Solve optimization problem (38) for shock-aligned mesh and DG solution on current slab
 - 7: **Extract spatial mesh from top of time slab:** Update $\bar{\mathcal{E}}_{x,h}$ by extracting the spatial mesh from the top of the (physical) space-time slab mesh \mathcal{E}_h (Section 3.1)
 - 8: **Update time:** Update t from the top of the (physical) space-time slab mesh
 - 9: **end while**
-

5. Numerical experiments

In this section, we formulate six problems (three conservation laws) to demonstrate the convergence, accuracy, and overall merit of the proposed slab-based implicit shock tracking approach via direct comparisons to exact solutions (if available) and popular shock capturing methods.

5.1. Inviscid Burgers' equation

We consider the time-dependent, inviscid Burgers' equation that governs nonlinear advection of a scalar quantity $w : \Omega_x \rightarrow \mathbb{R}$ through an d' -dimensional domain $\Omega_x \subset \mathbb{R}^{d'}$

$$\frac{\partial}{\partial t} w(x, t) + \nabla_x \cdot ((w(x, t)^2/2)\beta^T) = 0, \quad w(x, 0) = w_0(x) \quad (46)$$

for $x \in \Omega_x$, $t \in \mathcal{T}$, where $w_0 : \Omega_x \mapsto \mathbb{R}$ is the initial condition, $\beta \in \mathbb{R}^{d'}$ is the flow direction, and the boundary conditions are consistent with the initial condition at inflow boundaries. Burgers' equation is cast as a conservation law of the form (1) and the projected inviscid flux Jacobian and its eigenvalue decomposition are given in Appendix A. From this information, the transformed space-time version of the conservation law (including Riemann solver-based numerical flux) follows systematically from Section 2.2-2.3.

5.1.1. One-dimensional accelerating shock leaving domain

First, we consider Burgers' equation (46) ($\beta = 1$) with an accelerating shock in the one-dimensional spatial domain $\Omega_x := (-0.2, 1)$ and temporal domain $\mathcal{T} := (0, 1)$ produced by the initial condition

$$w_0 : x \mapsto \mu_1 H(-x) - \mu_2 H(x), \quad (47)$$

where $H : \mathbb{R} \rightarrow \mathbb{R}$ is the Heaviside function, and $\mu_1 = 4$ and $\mu_2 = 3$ in this work. The analytical solution is

$$w : (x, t) \mapsto \mu_1 H(x_s(t) - x) + \frac{\mu_2(x-1)}{1 + \mu_2 t} H(x - x_s(t)) \quad (48)$$

where $x_s : \mathcal{T} \rightarrow \mathbb{R}$ is the shock speed

$$x_s : t \mapsto (\mu_1/\mu_2 + 1)(1 - \sqrt{1 + \mu_2 t}) + \mu_1 t. \quad (49)$$

For the case considered, the shock leaves the domain before the end of the time interval of interest. Optimal convergence of the HOIST method for this problem (single slab) has been demonstrated in previous work

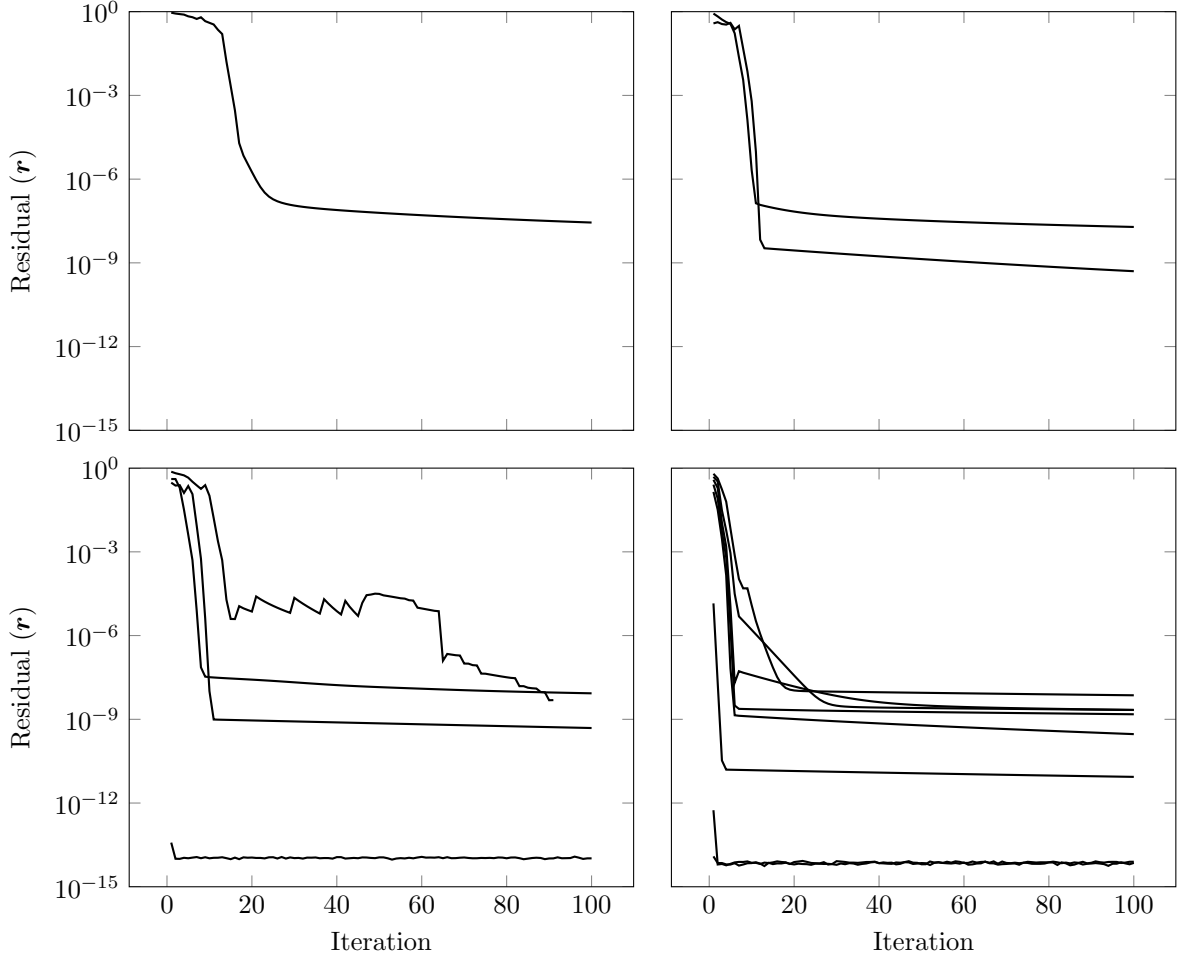


Figure 9: Convergence of the HOIST method for the accelerating shock problem with different slab configurations with $S = 1$ (top left), $S = 2$ (top right), $S = 4$ (bottom left), and $S = 8$ (bottom right) slabs. Different lines on a single plot correspond to the convergence history of different slabs.

[20] and will not be repeated here. The purpose of this numerical experiment is to demonstrate the space-time slab-based HOIST method and shock boundary condition approach for a simple problem, examine convergence of the optimization solver, and investigate performance with a different number of slabs.

We consider the convergence of the HOIST solver as a function of slab height. To this end, we consider slab heights of $\Delta t \in \{1.2, 0.6, 0.3, 0.15\}$, which corresponds to S slabs, where $S \in \{1, 2, 4, 8\}$. Because the slab height is optimized (Section 4.1), Δt is the initial height as the actual slab height changes during the optimization. We use a grid with 192 quadratic ($p = q = 2$) space-time simplices, which corresponds to $192/S$ elements per slab. All slabs are run for 100 iterations and the convergence of the DG residual is shown in Figure 9. As more slabs are added, the residuals converge more rapidly and to deeper tolerances, indicating the shock tracking problem is simpler for smaller slabs. The last slab for $S = 4$ and last three slabs for $S = 8$ correspond to times after the shock has left the domain, which is the reason the corresponding residuals are immediately machine zero. The solution field and space-time mesh for the $S = 8$ is shown in Figure 10. The curved shock is tracked by the quadratic mesh elements until it exits the domain in the fifth slab, where the translating boundary (Section 4.1) adjusts the upper temporal boundary such that the point where the shock exists the right boundary is exactly tracked.

Next, we solve the same problem with $S = 5$ slabs using the shock boundary condition approach [19] (Section 4.6). The first space-time slab is generated by extruding spatial mesh with 6 elements to produce a space-time mesh with 24 elements and implicit shock tracking is used to align it with the accelerating shock. The elements to the left of the shock are removed and the remaining domain is extruded to form the next

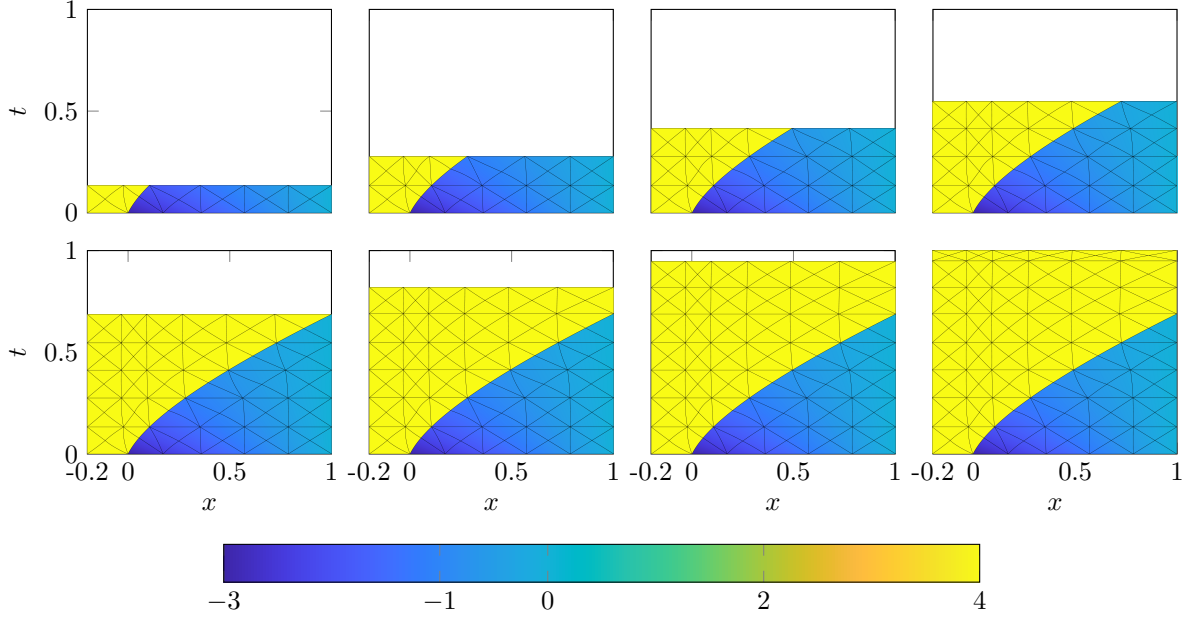


Figure 10: HOIST solution of accelerating shock inviscid Burgers' problem over a sequence of space-time slabs ($S = 8$).

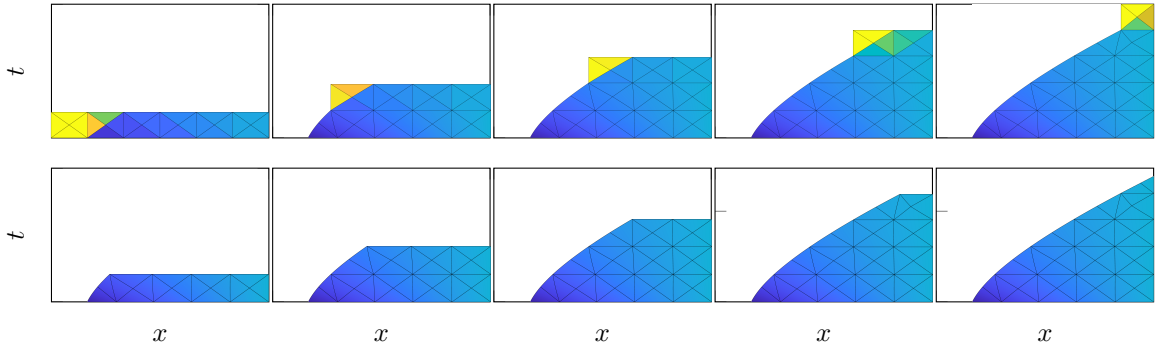


Figure 11: HOIST solution of accelerating shock inviscid Burgers' problem with the shock boundary condition approach (Section 4.6) including the initial (*top row*) and converged (*bottom row*) mesh and flow solution. Colorbar in Figure 10.

space-time slab. Because the state to the left of the shock is known, it is applied as a boundary condition to the leftmost elements. All deformation degrees of freedom associated with the shock boundary are free so it can move as necessary to track the discontinuity as it propagates in space-time. This process is repeated until the shock leaves the domain (Figure 11). This approach eliminates over half of the space-time elements and simplifies the shock tracking problem, which improves efficiency of the simulation.

5.1.2. One-dimensional shock formation and merge

Next, we consider a Burgers' equation (46) ($\beta = 1$) problem with a smooth initial condition that forms two distinct shock waves that eventually merge. The spatial domain is $\Omega_x := (-1, 1)$ and temporal domain is $\mathcal{T} := (0, 1)$ with initial condition

$$w_0 : x \mapsto 1.2 \exp\left(-\frac{(x + 0.5)^2}{0.025}\right) - \exp\left(-\frac{(x - 0.5)^2}{0.025}\right). \quad (50)$$

We use this problem to demonstrate the ability of the slab-based HOIST method to resolve shock formation and intersection. We also show mesh adaptation (Section 4.5) in the HOIST method helps adequately resolve the shock formation, i.e., the point at which the continuous features abruptly become discontinuities (wave

steepening).

To study adaptive mesh refinement, we consider a single slab $S = 1$ with a mesh of 96 quadratic ($p = q = 2$) space-time triangles. Space-time singularities form as the continuous features steepen into shocks. The adaptive refinement procedure increases resolution in these regions of the domain with minimal refinement in regions where the flow is well-resolved after eight rounds of mesh refinement (Figure 12). The converged, fully adapted mesh contains 207 triangles, and compares well to a reference solution computed with a highly refined second-order finite volume scheme at a temporal slice immediately before shock formation (Figure 13).

5.1.3. Propagating, curved shock in two dimensions

Finally, we consider Burgers' equation (46) ($\beta = (1, 0)$) with a quadratic initial condition [41]

$$w_0 : (x_1, x_2) \mapsto \begin{cases} (\frac{4}{3}(x_1 + 0.75))(0.5 - 2(x_2^2 - 0.25)) & x \in (-1, 0) \times (-0.5, 0.5) \\ 0 & \text{else} \end{cases} \quad (51)$$

over the two-dimensional spatial domain $\Omega_x := (-1, 1)^2$ and temporal domain $\mathcal{T} := (0, 1.5)$. The initial condition is a straight-sided shock with a quadratically varying conserved variable, which causes the shock to curve as it propagates.

We use the slab-based HOIST method with $S = 3$ slabs. The spatial domain is discretized with 32 triangular elements, which are extruded and split to form an initial slab with 448 quadratic ($p = q = 2$) space-time tetrahedral elements. As time evolves, the initially straight-sided shock begins to obtain a curved profile, which is captured by the $q = 2$ elements (Figure 14) and the $p = 2$ solution approximation accurately resolves the conserved variable.

5.2. Shallow water equations

Next we consider flow of an incompressible, inviscid, non-heat conducting fluid subject to gravitational forces, but neglecting vertical acceleration through a domain $\Omega_x \subset \mathbb{R}^d$ over a time interval $\mathcal{T} \subset \mathbb{R}_{\geq 0}$, which is governed by the shallow water equations (SWE)

$$\begin{aligned} \frac{\partial}{\partial t} \rho(x, t) + \frac{\partial}{\partial x_j} \rho(x, t) v_j(x, t) &= 0 \\ \frac{\partial}{\partial t} (\rho(x, t) v_i(x, t)) + \frac{\partial}{\partial x_j} (\rho(x, t) v_i(x, t) v_j(x, t) + \delta_{ij} \rho(x, t)^2 / 2) &= g \rho(x, t) \frac{\partial h}{\partial x_i}(x) \end{aligned} \quad (52)$$

for $i = 1, \dots, d'$. The geopotential $\rho(\cdot, t) : \Omega_x \rightarrow \mathbb{R}_{>0}$ and fluid velocity $v(\cdot, t) : \Omega_x \rightarrow \mathbb{R}^d$ are implicitly defined as the solution to (52). The geopotential is related to the total depth of the fluid $H(\cdot, t) : \Omega_x \rightarrow \mathbb{R}_{>0}$ as

$$\rho(x, t) = gH(x, t), \quad H(x, t) = \eta(x, t) + h(x) \quad (53)$$

where $g \in \mathbb{R}_{>0}$ is the gravitational acceleration and the total depth of the fluid is written as the summation of the channel bed depth $h : \Omega_x \rightarrow \mathbb{R}_{>0}$ and the height of the free surface $\eta(\cdot, t) : \Omega_x \rightarrow \mathbb{R}_{>0}$. The shallow water equations are cast as a conservation law of the form (1) and the projected inviscid flux Jacobian and its eigenvalue decomposition are given in Appendix A. From this information, the transformed space-time version of the conservation law (including Riemann solver-based numerical flux) follows systematically from Section 2.2-2.3.

We consider the canonical one-dimensional ($d' = 1$) dam break problem with $g = 1$ and no bathymetry ($h(x) = 0$) over $\Omega_x := (-5, 5)$ and time interval $\mathcal{T} := (0, 6)$, which is a Riemann problem for the SWE (52) with initial condition

$$\eta(x, 0) = \begin{cases} 3 & x \in [-5, 0) \\ 1 & x \in (0, 5] \end{cases}, \quad v(x, 0) = 0. \quad (54)$$

At both boundaries, we assume a non-penetration condition, i.e., $v(x, t) \cdot \eta_x(x) = 0$, where $\eta_x \in \mathbb{S}^d$ is the outward unit normal to the boundary. As such, this problem features two waves—a shock and rarefaction—that propagate from the origin and reflect off the boundaries. This numerical experiment will demonstrate the slab-based space-time HOIST method for the SWE and its ability to resolve wave reflections.

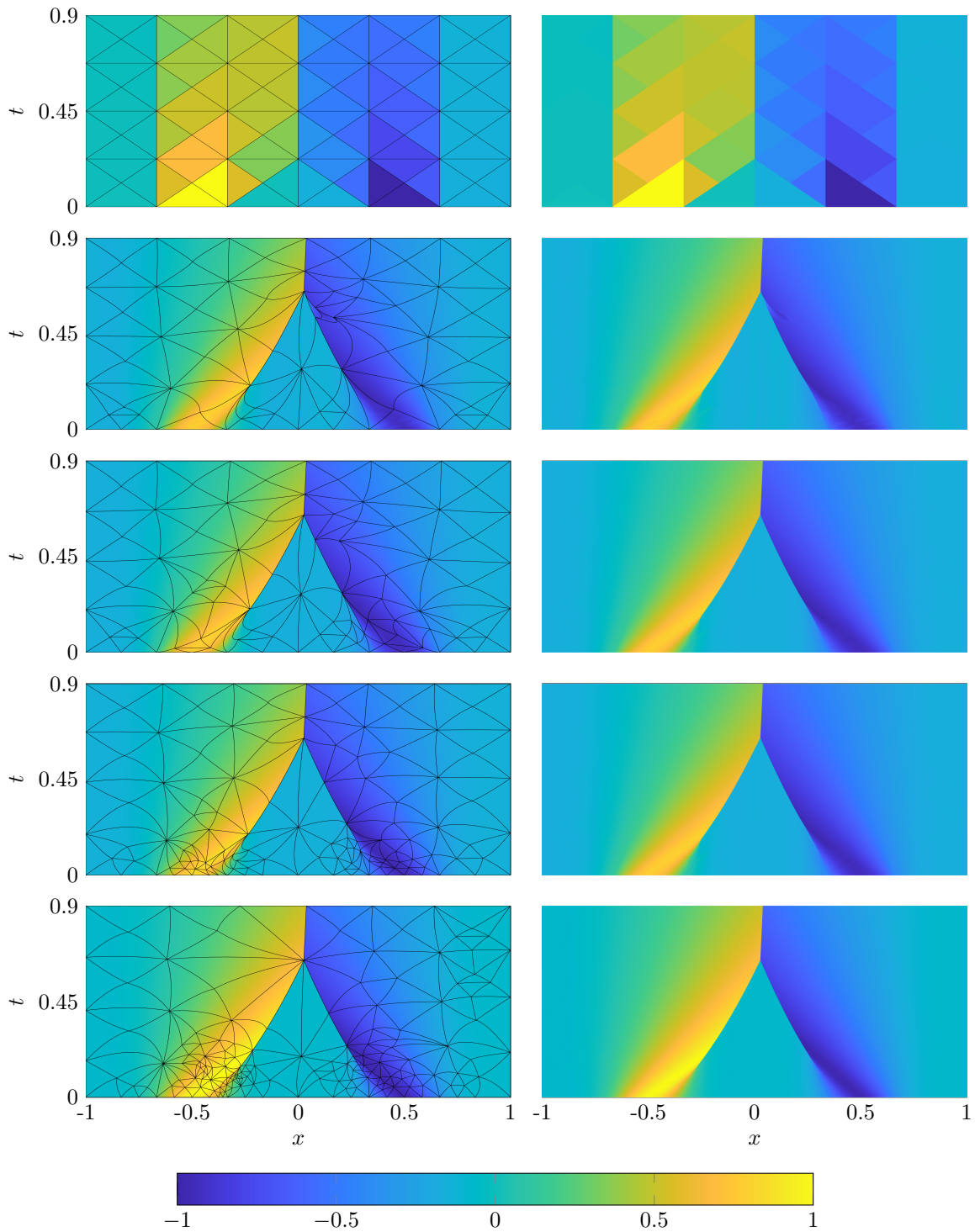


Figure 12: HOIST solutions for the inviscid Burgers' problem with shock formation including the initial mesh and flow solution (top row), as well as the mesh and flow solution after one (second row), two (third row), four (fourth row), and eight (fifth row) rounds of adaptive mesh refinement.

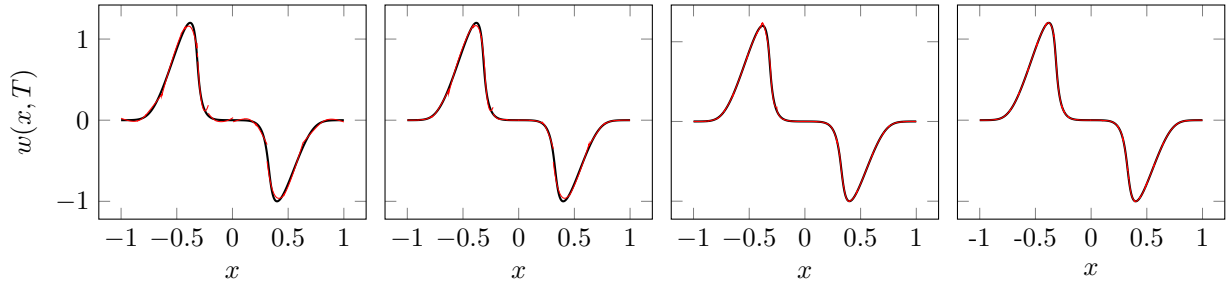


Figure 13: HOIST solution (—) for the inviscid Burgers' problem with shock formation at temporal slices $t = 0.1$ (just before shock formation) after one (*left*), two (*middle left*), four (*middle right*), and eight (*right*) rounds of adaptive mesh refinement. A reference solution computed with a highly refined second-order finite volume method is shown in (—).

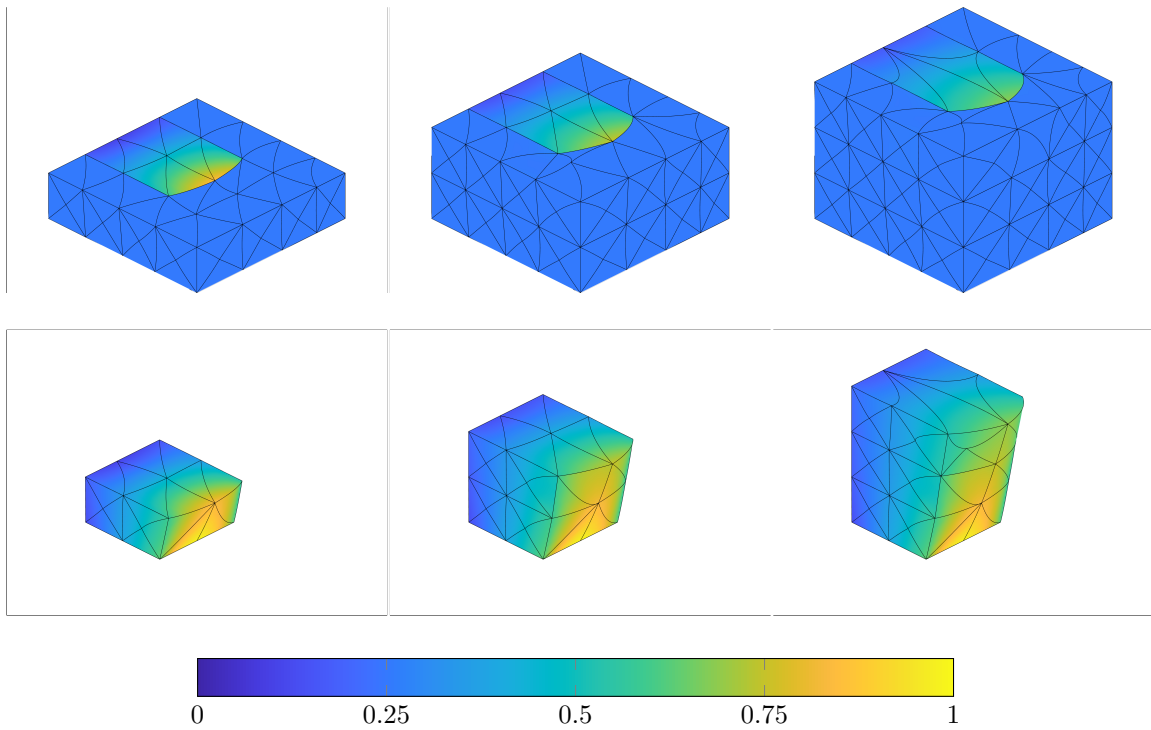


Figure 14: Slab-base HOIST solution to the two-dimensional inviscid Burgers' problem.

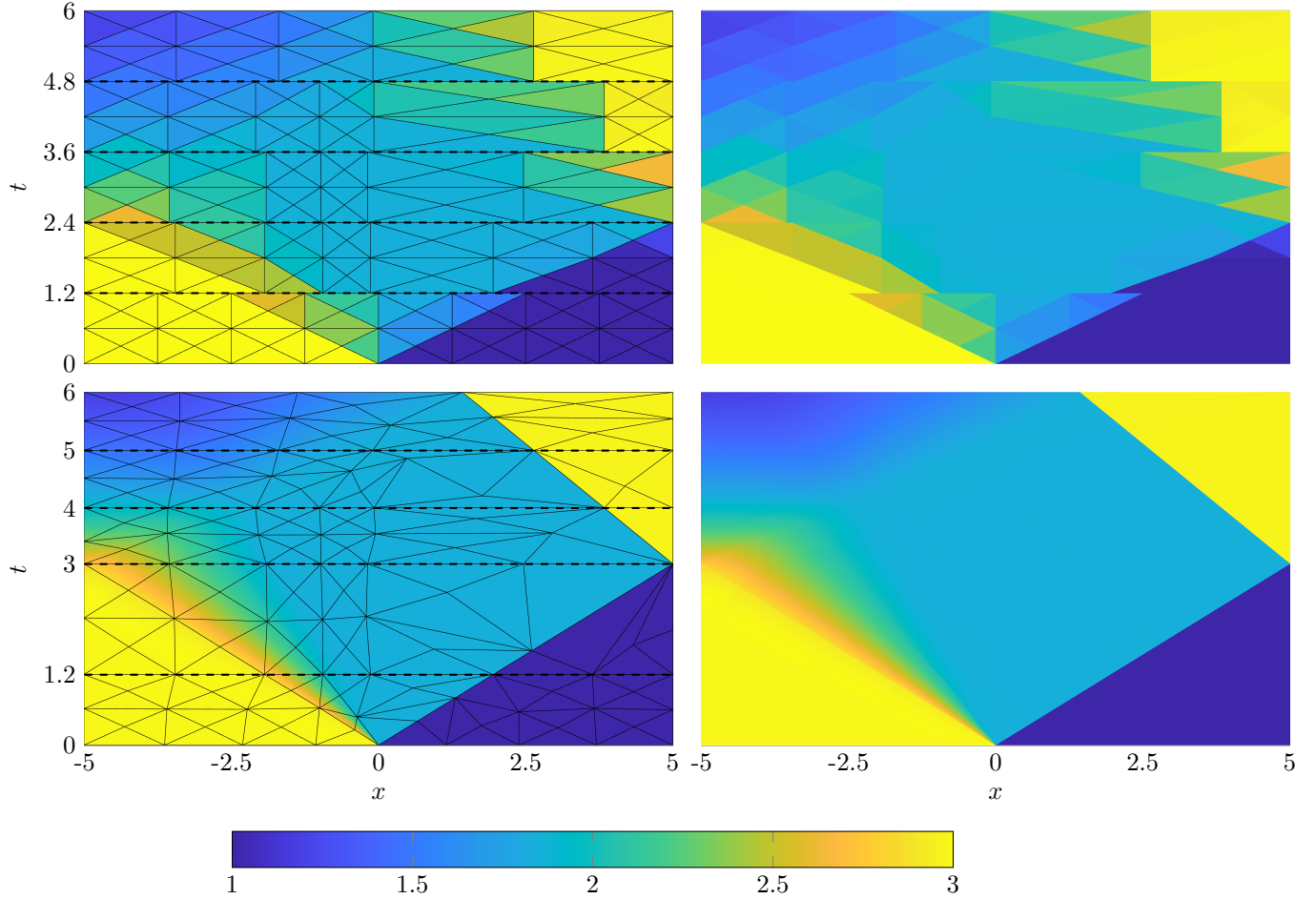


Figure 15: Slab-based HOIST solution (geopotential) of the SWE including the initial (*top row*) and converged (*bottom row*) mesh and flow solution. The interface between each slab is denoted by (---) in both the initial solution and tracked solution.

This problem is discretized using 5 slabs and solved using the space-time HOIST method. The first slab is generated from a spatial mesh with 8 elements, which are extruded and split to produce 32 space-time linear ($q = 1$) triangles with a quadratic ($p = 2$) solution approximation. As shown in Figure 15, in the first slab, the shock and head/tail of the rarefaction are successfully tracked as they propagate away from the origin. In the second slab, the space-time points at which the shock and rarefaction reflect off the wall are tracked by means of the variable temporal boundary (Section 4.1), i.e., the second slab is stretched in time such that these intersections are represented perfectly. Because of this, the second slab covers more of the temporal domain than the first slab while still accurately approximating the flow field. In subsequent slabs, the shock and rarefaction are reflected and propagate in the reflected directions until the end of the temporal domain is reached by the fifth slab.

Remark 12. Figure 15 (*top row*) shows the initial solution and mesh for each slab in the space-time solution. The initial mesh is guaranteed to be conforming to the converged mesh and solution from the previous slab (Figure 15 (*bottom row*)), but the initial meshes for each slab interface are not guaranteed to be conforming (as shown). The initial meshes are never used simultaneously so conformity is irrelevant. This remark also applies to Figures 16 and 19.

5.3. Euler equations of gasdynamics

Finally, we consider flow of an inviscid, compressible fluid through a domain $\Omega_x \subset \mathbb{R}^{d'}$, which are governed by the Euler equations

$$\begin{aligned} \frac{\partial}{\partial t} \rho(x, t) + \frac{\partial}{\partial x_j} (\rho(x, t) v_j(x, t)) &= 0 \\ \frac{\partial}{\partial t} (\rho(x, t) v_i(x, t)) + \frac{\partial}{\partial x_j} (\rho(x, t) v_i(x, t) v_j(x, t) + P(x, t) \delta_{ij}) &= 0 \\ \frac{\partial}{\partial t} (\rho(x, t) E(x, t)) + \frac{\partial}{\partial x_j} ([\rho(x, t) E(x, t) + P(x, t)] v_j(x, t)) &= 0 \end{aligned} \quad (55)$$

for all $x \in \Omega_x$ and $t \in \mathcal{T} \subset \mathbb{R}$, where $i = 1, \dots, d'$ and summation is implied over the repeated index $j = 1, \dots, d'$. The density of the fluid $\rho : \Omega_x \times \mathcal{T} \rightarrow \mathbb{R}_{>0}$, the velocity of the fluid $v_i : \Omega_x \times \mathcal{T} \rightarrow \mathbb{R}$ in the x_i direction for $i = 1, \dots, d'$, and the total energy of the fluid $E : \Omega_x \times \mathcal{T} \rightarrow \mathbb{R}_{>0}$ are implicitly defined as the solution of (55). For a calorically ideal fluid, the pressure of the fluid, $P : \Omega_x \times \mathcal{T} \rightarrow \mathbb{R}_{>0}$ is related to the energy via the ideal gas law

$$P = (\gamma - 1)(\rho E - \rho v_i v_i / 2) \quad (56)$$

where $\gamma \in \mathbb{R}_{>0}$ is the ratio of specific heats. The Euler equations are cast as a conservation law of the form (1) and the projected inviscid flux Jacobian and its eigenvalue decomposition are given in [Appendix A](#). From this information, the transformed space-time version of the conservation law (including Riemann solver-based numerical flux) follows systematically from [Section 2.2-2.3](#).

5.3.1. Sod's shock tube

Sod's shock tube is a Riemann problem for the Euler equations that models an idealized shock tube where the membrane separating a high pressure region from a low pressure one is instantaneously removed. This is a commonly used validation problem since it has an analytical solution that features a shock wave, rarefaction wave, and contact discontinuity. The flow domain is $\Omega_x := (0, 1)$, the time domain is $\mathcal{T} := (0, 1)$, and the initial condition is given in terms of the density, velocity, and pressure as

$$\rho(x, 0) = \begin{cases} 1 & x < 0.5 \\ 0.125 & x \geq 0.5 \end{cases}, \quad v(x, 0) = 0, \quad P(x, 0) = \begin{cases} 1 & x < 0.5 \\ 0.1 & x \geq 0.5 \end{cases}. \quad (57)$$

Wall boundary conditions are prescribed at both $x = 0$ and $x = 1$, i.e., $v(x, t) \cdot \eta_x(x) = 0$, where $\eta_x \in \mathbb{S}^{d'}$ is the outward unit normal to the boundary, which means any waves that reach the boundary will reflect back into the domain. The solution of this problem contains three waves (shock, contact, rarefaction) that emanate from $x = 0.5$ at $t = 0$ and propagate until the shock and rarefaction reflect off the walls. The shock and contact eventually interact creating a pass through, reflection, and intermediate that continue to interact with one another and the right wall. Eventually the reflected rarefaction interacts with the shock causing it to curve. The time domain considered in this work is five times longer than the one usually associated with this problem [47] to induce these interactions. The purpose of this numerical experiment is to demonstrate the slab-based space-time HOIST method is able to track various types of non-smooth features and locate triple points without seeding with *a priori* information.

This problem is discretized with $S = 6$ slabs and solved using the space-time HOIST method. An unstructured space-time mesh of 65 linear ($q = 1$) simplices with quadratic solution approximation ($p = 2$) is used for the first slab. Subsequent space-time slabs are generated using the approach described in [Section 3](#) whereby the spatial mesh at the end of a time slab is extruded and split into simplices. All of the solution features described above are tracked by the slab-based HOIST method ([Figure 16](#)) in various slabs. The shock, contact, and head/tail of the rarefaction are all tracked in the first slab, which shows the method can locate multiple non-smooth features intersecting at a generalized triple point. This is demonstrated again at later times when various shock-shock and shock-contact interactions occurs. Furthermore, the variable temporal boundary allows the method to track shock (top of slab 3) and rarefaction (top of slab 4) reflections off the walls, as well as the shock-contact interaction (top of slab 4). [Figure 17](#) shows several spatial solutions at given points in time for the HOIST method and a reference solution (second-order finite

volume method with superbee limiter on a grid with over 10^5 elements and fourth-order Runge-Kutta time integration with adaptive time steps). The slices in time display relevant shock dynamics and the ability of HOIST to represent the shock fronts as perfect discontinuities both before and after wave interactions.

The reflected shock and contact intersect at nearly (but not exactly) the same time as the rarefaction reflects off the wall. For the coarse mesh used, the translating temporal slab is insufficient to track both features, and the HOIST method chose to track the shock-contact interaction because it is the stronger feature. Thus, the interaction of the rarefaction with the left wall is an approximation (Figure 18). Two options to resolve this issue are to use a: 1) finer mesh (possibly with h -adaptation) or 2) more flexible parametrization of the upper temporal boundary. To demonstrate the flexibility of HOIST, we consider the latter by allowing free temporal motion of the nodes on the top of the fourth space-time slab, similar to parametrization of shock boundaries (Section 4.6). This is dangerous because causality may be violated if the relative motion of two adjacent nodes is too several, in which case the solution in the current slab would depend on the solution in the next slab. However, for this problem, the approach works robustly without causality violated and allows the rarefaction reflection and shock-contact interaction to be tracked simultaneously on the coarse grid (Figure 18). Future work will push this approach further with additional constraints to enforce causality.

5.3.2. Shu-Osher problem

The Shu-Osher problem is a one-dimensional idealization of shock-turbulence interaction in which a shock propagates into a density field with artificial fluctuations. This phenomena is modeled by the ideal gas one-dimensional Euler equations, i.e., (55) with $d' = 1$, with $\gamma = 1.4$. The flow domain is $\Omega_x := (-5, 5)$ and temporal domain is $\mathcal{T} := (0, T)$ with $T = 2$. The initial condition for the flow is

$$(\rho(x, 0), v(x, 0), P(x, 0)) = \begin{cases} (3.857143, 2.629369, 10.3333) & x < -4 \\ (1 + 0.2 \sin(5x), 0, 1) & x \geq -4 \end{cases}$$

with a supersonic inlet at $x = -5$ that prescribes the density, velocity, and pressure

$$(\rho(-5, t), v(-5, t), P(-5, t)) = (3.857143, 2.629369, 10.3333)$$

and a solid wall at $x = 5$. This problem corresponds to a Mach $M = 3$ shock moving into a field with a small density (or entropy) disturbance. As time progresses, the fluctuations that have passed through the discontinuity become more oscillatory and eventually steepen into shocks. The final time ($T = 2$) is chosen larger than often seen in the literature [41, 11, 43, 21] to expose these challenging features. The purpose of this numerical experiment is to demonstrate the slab-based space-time HOIST method can simultaneously resolve strong shocks and weak shocks, shock formation, and fluctuations that can easily be washed out by numerical or artificial dissipation. This problem will also demonstrate the benefit of using adaptive mesh refinement (Section 4.5) and shock boundary conditions (Section 4.6).

This problem is initially solved using the slab-based space-time HOIST method with $S = 5$ slabs. The initial slab is generated by extruding a spatial mesh of 20 elements and splitting the quadrilaterals to produce 160 quadratic ($p = q = 2$) space-time simplices. Subsequent slabs are generated using the approach in Section 3. The purpose of this initial simulation is to approximately track the main discontinuity so shock boundary conditions can be used. As such, the HOIST method is terminated once a weak optimality tolerance ($\epsilon = 10^{-8}$) is satisfied or after 200 SQP iterations. This leads to accurate representation of the main shock; however, the oscillations and weaker shocks are not resolved (Figure 19). Next, the mesh is uniformly refined and the region of the domain upstream of the shock, where the solution is known analytically, is removed, which reduces the elements in the mesh from 3184 elements to 1500 elements. Finally, the space-time HOIST method is applied to this reduced problem with adaptive mesh refinement and shock boundary conditions, which allows the finer features (shock formation and post-shock oscillation) to be represented accurately (Figure 20). The HOIST solution at the final time $T = 2$ shows excellent agreement with a reference solution (second-order finite volume method with superbee limiter on a grid with over 5×10^4 and fourth-order Runge-Kutta time integration with adaptive time steps) everywhere except a few spatial locations (Figure 21). The relative L^2 error norm of the HOIST solution compared to the reference solution at final time $T = 2$ is 3.97×10^{-4} .

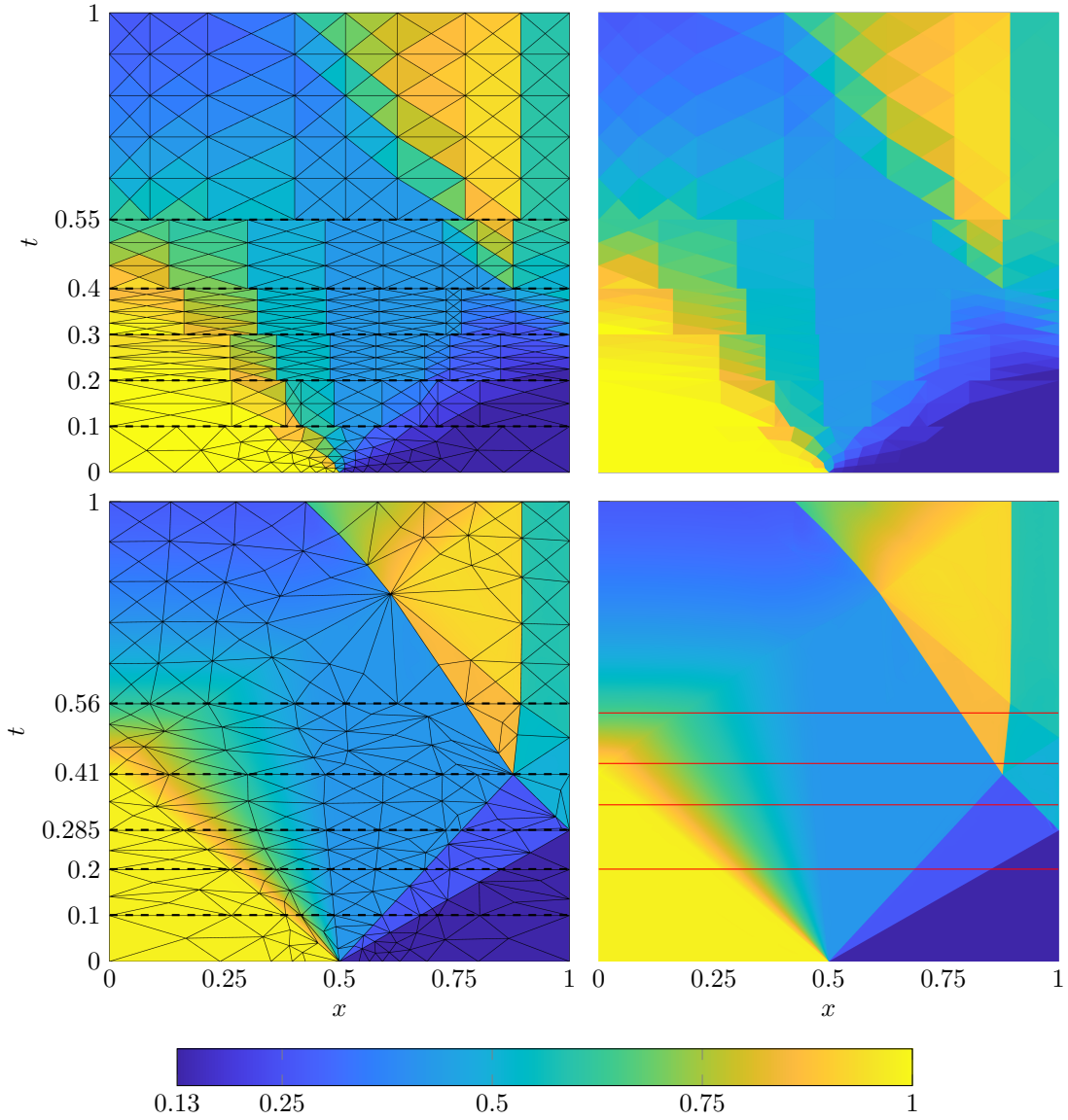


Figure 16: Slab-based HOIST solution (density) of Sod's shock tube including the initial (*top row*) and converged (*bottom row*) mesh and flow solution. The interface between each slab is denoted by (---) in both the initial solution and tracked solution. Slices through the domain indicated by (—) at times near shock interactions can be seen in Figure 17.

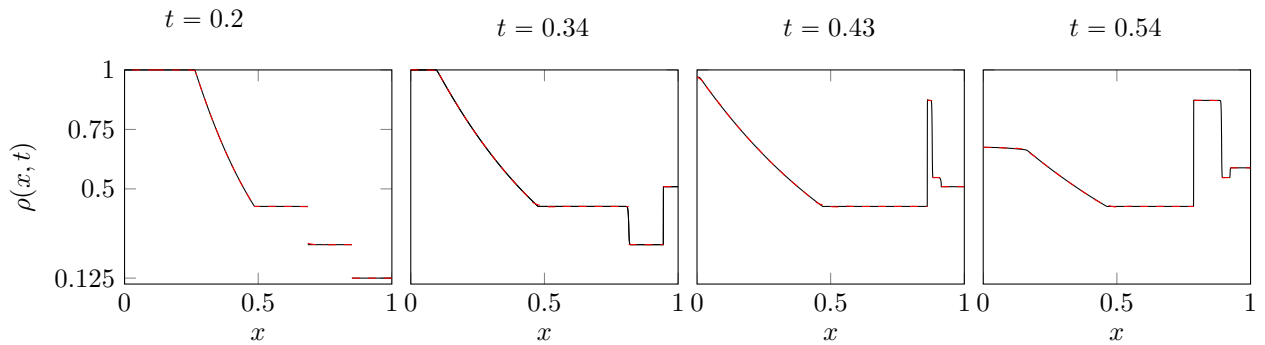


Figure 17: Slab-based HOIST solution slices (density) (---) of Sod's shock tube compared against the reference solution (—) at times indicated by (—) in Figure 16.

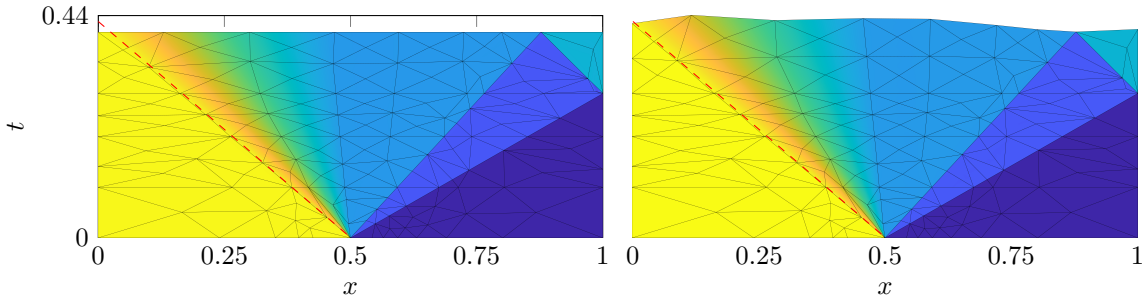


Figure 18: Slab-based HOIST solution (first four slabs) to Sod's shock tube using the translating boundary (*left*) and a more general parametrization of the upper temporal boundary (*right*). The true rarefaction trajectory is identified with (---). Colorbar in Figure 16.

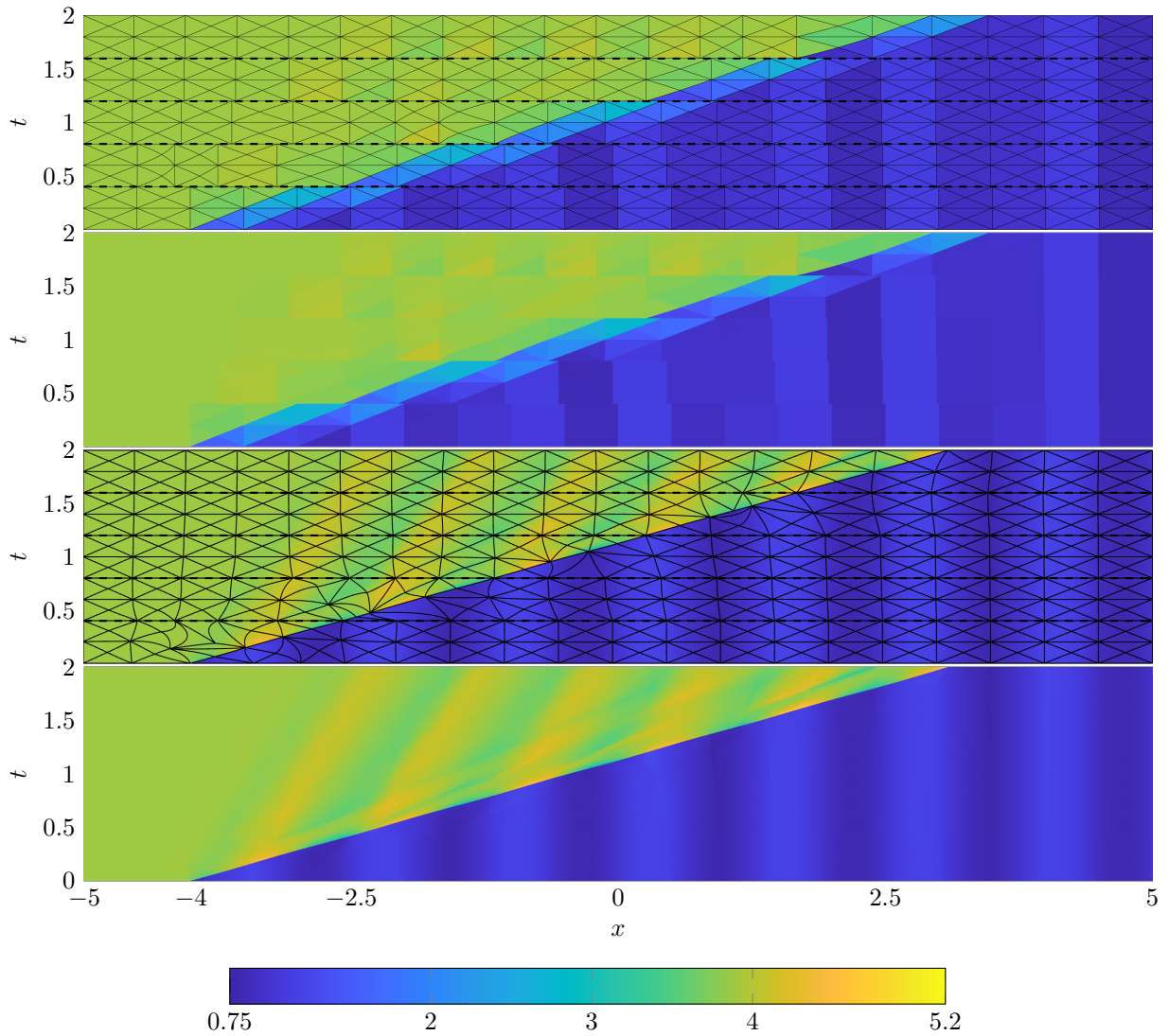


Figure 19: Slab-based HOIST solution (density) for the Shu-Osher problem, including the initial (*top two rows*) and converged (*bottom two rows*) mesh and flow solution. The interface between each slab is denoted by (---) in both the initial solution and tracked solution.

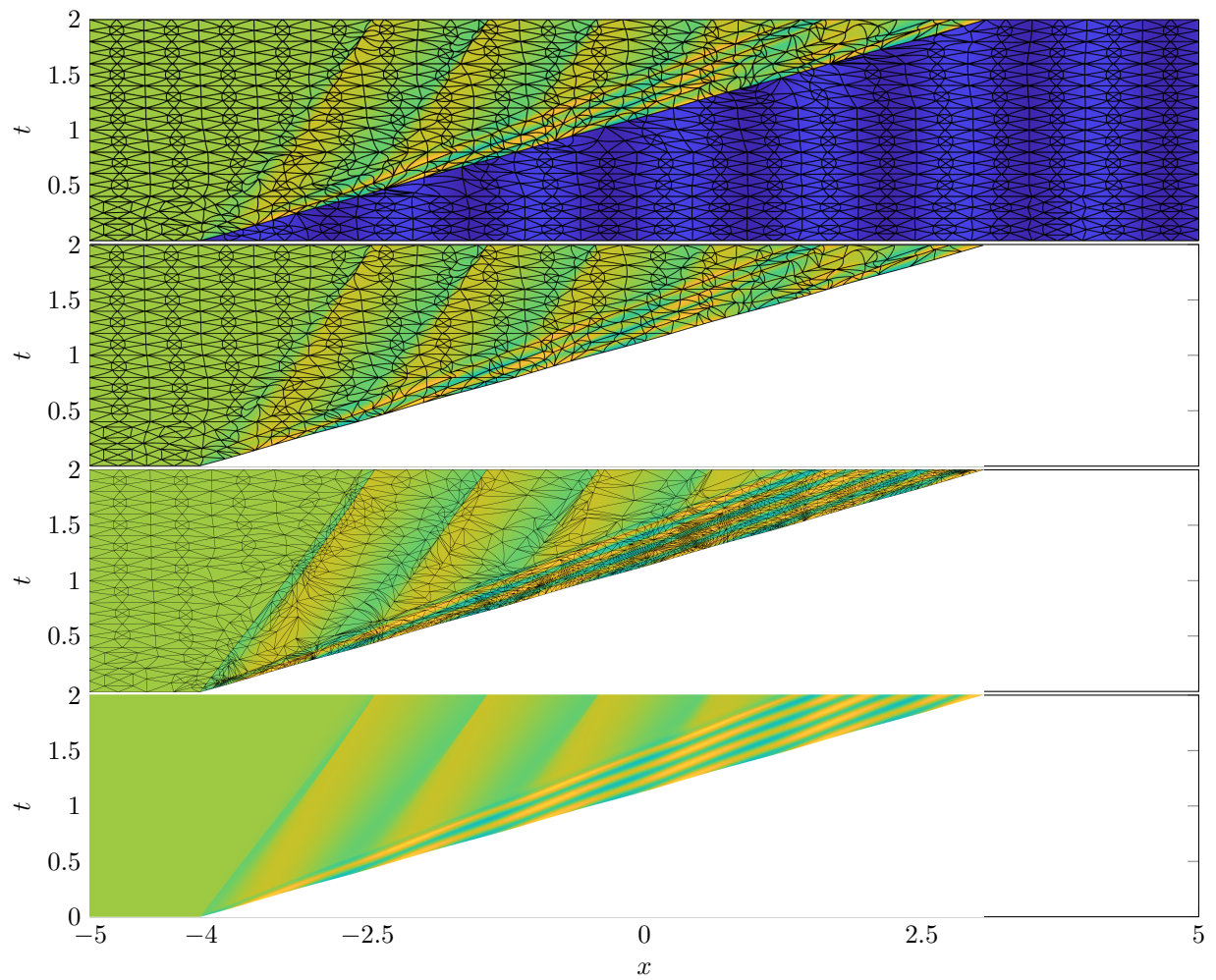


Figure 20: HOIST solution for the Shu-Osher problem after uniform mesh refinement (*top row*), removing the region of the mesh with known solution (*second row*), and using adaptive mesh refinement (*bottom two rows*). Colorbar in Figure 19.

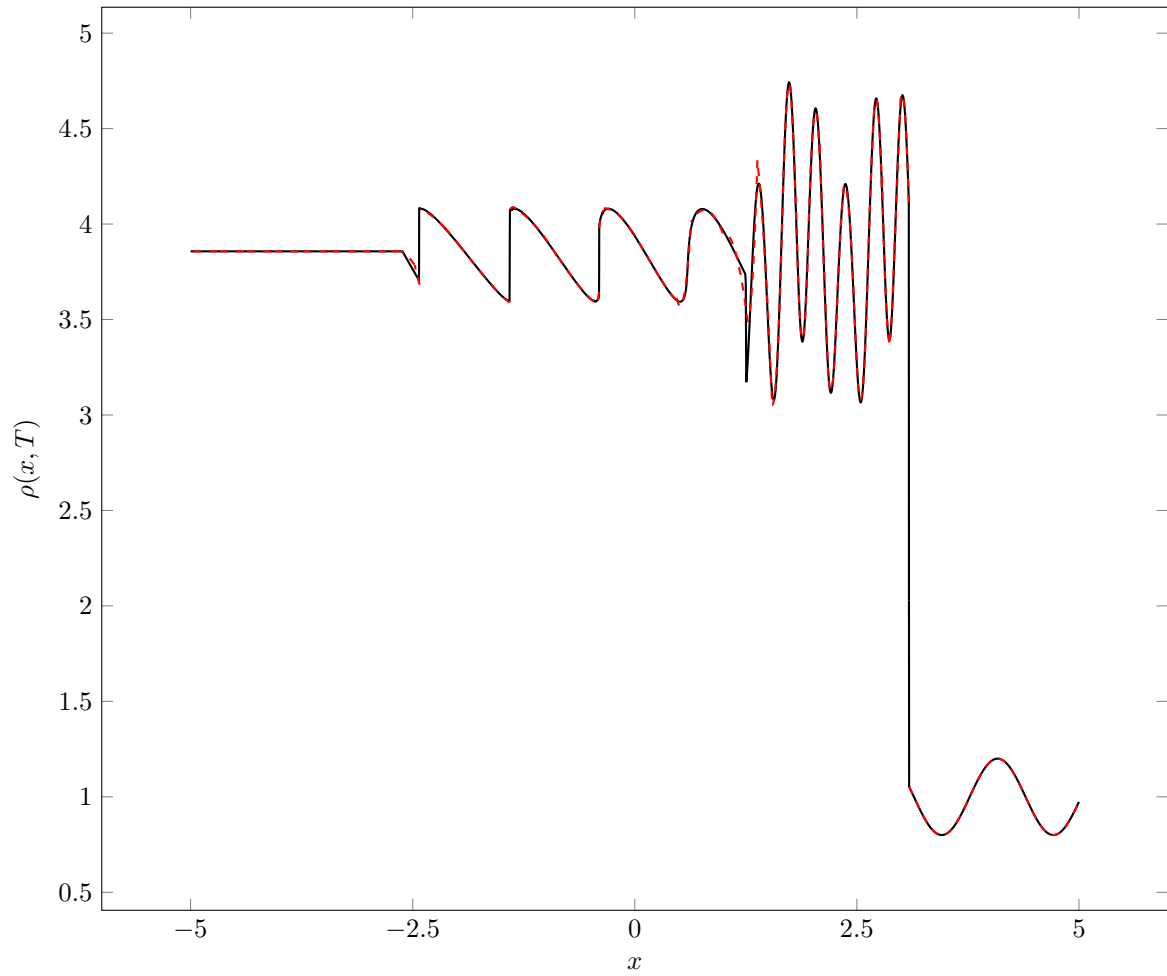


Figure 21: Time slice of HOIST solution (density) on adapted mesh (---) and a reference solution (—) at $T = 2$.

6. Conclusion

High Order Implicit Shock Tracking (HOIST) is a method that approximates solutions of conservation laws by a DG discretization of a conservation law to represent non-smooth features with inter-element jumps, while smooth regions of the flow are approximated using high-order polynomials, which eliminates the need for stabilization techniques (e.g., limiting and artificial viscosity) commonly used for shock capturing. Shock-aligned meshes are produced as the solution of an optimization problem over the DG state vector and nodal coordinates of the grid.

In this work, we extend the HOIST method to time-dependent problems using a slab-based space-time approach. This is achieved by reformulating a time-dependent conservation law in d' dimensions as steady conservation law in $d' + 1$ dimensions and applying the HOIST method of [59, 20]. By systematically building a transformed space-time conservation law from a time-dependent conservation law, the flux function, source term, and numerical flux function can be explicitly expressed in terms of the well-known spatial counterparts (Section 2). To avoid computations over the entire time domain and unstructured mesh generation in $d' + 1$ dimensions, we introduce a general procedure to generate conforming, simplex-only meshes of space-time slabs in such a way that preserves features (e.g., curved elements, refinement regions) from previous time slabs (Section 3). In addition to avoiding global temporal coupling, space-time slabs also reduce the difficulty of the shock tracking problem, especially for problems with complex interactions that evolve over time.

While the space-time HOIST method is formulated exactly as the original HOIST method [59] over the space-time slab, several practical adaptations proved beneficial in the space-time setting including 1) a translating temporal boundary (Section 4.1), 2) nondimensionalization of a space-time slab (Section 4.4), 3) adaptive mesh refinement (Section 4.5), and 4) shock boundary conditions (Section 4.6). Several numerical experiments demonstrate the proposed space-time HOIST method provides highly accurate solutions of conservation laws on coarse space-time grids and is sufficiently robust to accurately track and resolve straight-sided non-smooth features (rarefactions, contact discontinuities, shock waves) curved shocks, shock formation, shock-shock and shock-boundary interactions, and triple points.

Future research directions include extending this methods to more complex and higher dimensional problems. This will require parallelization of the HOIST solver, likely via domain decomposition, and suitable preconditioners for the linearize HOIST optimality system. Additionally, the extrude-then-split approach proposed in this work applies in any dimension d ; however, become inefficient in $d = 3$ and impractical in $d = 4$ because of the larger number of simplices required for a conforming split of a prism ($N_3 = 14$, $N_4 = 58$). Several approaches should be investigated to circumvent this: 1) a global splitting algorithm like [53] to reduce the N_d factor and produce a conforming simplex-only mesh, 2) more efficient local splittings that do not guarantee conforming simplex-only meshes with non-conforming extension of the HOIST method, and 3) generalization of HOIST for non-simplex grids so (extruded) block or prism meshes can be used directly for shock tracking.

Appendix A. Projected inviscid flux Jacobians

In this section, we formulate the three conservation laws considered in this work in the generic form of (1) and present the inviscid flux Jacobians and their eigenvalue decompositions. The Jacobians and their eigenvalue decompositions were derived by hand for Burgers' equation and using MapleTM for the other equations.

Appendix A.1. Inviscid Burgers' equation

For the inviscid Burgers' equation (46), the solution vector, inviscid flux function, and source term take the form

$$U_x(x, t) = w(x, t), \quad \mathcal{F}_x(W_x) = (W_x^2/2)\beta^T, \quad \mathcal{S}_x(W_x) = 0, \quad (\text{A.1})$$

where the projected inviscid flux Jacobian and its eigenvalue decomposition are given by

$$B_x(W_x, \eta_x) = (\beta \cdot \eta_x)W_x, \quad V_x(W_x, \eta_x) = V_x(W_x, \eta_x)^{-1} = 1, \quad \Lambda_x(W_x, \eta_x) = (\beta \cdot \eta_x)W_x. \quad (\text{A.2})$$

Appendix A.2. Shallow water equations

For the shallow water equations (52), the solution vector, inviscid flux function, and source term take the form

$$U_x(x, t) = \begin{bmatrix} \rho(x, t) \\ \rho(x, t)v(x, t) \end{bmatrix}, \quad \mathcal{F}_x(W_x) = \begin{bmatrix} \check{\rho}\check{v}^T \\ \check{\rho}\check{v}^T + (\check{\rho}^2/2)I_{d'} \end{bmatrix}, \quad \mathcal{S}_x(W_x) = \begin{bmatrix} 0 \\ g\check{\rho}\nabla h(x) \end{bmatrix} \quad (\text{A.3})$$

where $W_x = (\check{\rho}, \check{\rho}\check{v})$. The projected inviscid flux Jacobian is given by

$$B_x(W_x, \eta_x) = \begin{bmatrix} 0 & \eta_x^T \\ \check{\rho}\eta_x - \check{v}_{\eta_x}\check{v} & \check{v}\eta_x^T + \check{v}_{\eta_x}I_{d'} \end{bmatrix}, \quad (\text{A.4})$$

where $\check{v}_{\eta_x} = \check{v} \cdot \eta_x$. In the $d' = 1$ case, the eigenvalue decomposition of the projected inviscid flux Jacobian is

$$\begin{aligned} \Lambda_x(W_x, \eta_x) &= \begin{bmatrix} \check{v}_{\eta_x} - \sqrt{\check{\rho}} & \\ & \check{v}_{\eta_x} + \sqrt{\check{\rho}} \end{bmatrix} \\ V_x(W_x, \eta_x) &= \begin{bmatrix} 1 & 1 \\ \check{v} - \sqrt{\check{\rho}}\eta_x & \check{v} + \sqrt{\check{\rho}}\eta_x \end{bmatrix} \\ V_x(W_x, \eta_x)^{-1} &= \frac{1}{2\check{\rho}} \begin{bmatrix} \check{v}_{\eta_x} + \sqrt{\check{\rho}} & -\eta_x^T \\ -\check{v}_{\eta_x} + \sqrt{\check{\rho}} & \eta_x^T \end{bmatrix} \end{aligned} \quad (\text{A.5})$$

whereas in the $d' = 2$ case, it takes the form

$$\begin{aligned} \Lambda_x(W_x, \eta_x) &= \begin{bmatrix} \check{v}_{\eta_x} - \sqrt{\check{\rho}} & & \\ & \check{v}_{\eta_x} & \\ & & \check{v}_{\eta_x} + \sqrt{\check{\rho}} \end{bmatrix} \\ V_x(W_x, \eta_x) &= \begin{bmatrix} 1 & 0 & 1 \\ \check{v} - \sqrt{\check{\rho}}\eta_x & g(\eta_x) & \check{v} + \sqrt{\check{\rho}}\eta_x \end{bmatrix} \\ V_x(W_x, \eta_x)^{-1} &= \frac{1}{2\check{\rho}} \begin{bmatrix} \check{v}_{\eta_x} + \sqrt{\check{\rho}} & -\eta_x^T \\ -2\sqrt{\check{\rho}}(\check{v} \cdot g(\eta_x)) & 2\sqrt{\check{\rho}}g(\eta_x)^T \\ -\check{v}_{\eta_x} + \sqrt{\check{\rho}} & \eta_x^T \end{bmatrix} \end{aligned} \quad (\text{A.6})$$

where $g(\eta_x) = (-(\eta_x)_2, (\eta_x)_1)$.

Appendix A.3. Euler equations of gasdynamics

For the Euler equations with ideal gas law (55), the solution vector, inviscid flux function, and source term take the form

$$U_x(x, t) = \begin{bmatrix} \rho(x, t) \\ \rho(x, t)v(x, t) \\ \rho(x, t)E(x, t) \end{bmatrix}, \quad \mathcal{F}_x(W_x) = \begin{bmatrix} \check{\rho}\check{v}^T \\ \check{\rho}\check{v}\check{v}^T + \check{P}I_{d'} \\ (\check{\rho}\check{E} + \check{P})\check{v}^T \end{bmatrix}, \quad \mathcal{S}_x(W_x) = 0 \quad (\text{A.7})$$

where $W_x = (\check{\rho}, \check{\rho}\check{v}, \check{\rho}\check{E})$ and $\check{P} = (\gamma - 1)(\check{\rho}\check{E} - \check{\rho}\check{v} \cdot \check{v}/2)$. The projected inviscid flux Jacobian is

$$B_x(W_x, \eta_x) = \begin{bmatrix} 0 & \eta_x^T & 0 \\ \left(\frac{\check{\gamma}-1}{2}\right)\|\check{v}\|^2\eta_x - \check{v}_{\eta_x}\check{v} & \check{v}_{\eta_x}I_{d'} + \check{v}\eta_x^T - (\check{\gamma}-1)\eta_x\check{v}^T & (\check{\gamma}-1)\eta_x \\ \left[\left(\frac{\check{\gamma}-1}{2}\right)\|\check{v}\|^2 - \check{H}\right]\check{v}_{\eta_x} & \check{H}\eta_x^T - (\check{\gamma}-1)\check{v}_{\eta_x}\check{v}^T & \check{\gamma}\check{v}_{\eta_x} \end{bmatrix} \quad (\text{A.8})$$

where $\check{v}_{\eta_x} = \check{v} \cdot \eta_x$ and $\check{H} = (\check{\rho}\check{E} + \check{P})/\check{\rho}$. The eigenvalues and right eigenvectors of the projected inviscid Jacobian are given by

$$\Lambda(W_x, \eta_x) = \begin{bmatrix} \check{v}_{\eta_x} - \check{c} & & \\ & \check{v}_{\eta_x} I_{d'} & \\ & & \check{v}_{\eta_x} + \check{c} \end{bmatrix}, \quad V_x(W_x, \eta_x) = \begin{bmatrix} 1 & & 1 \\ \check{v} - \check{c}\eta_x & (\check{v} - \eta_x)\eta_x^T + I_{d'} & \check{v} + \check{c}\eta_x \\ \check{H} - \check{v}_{\eta_x}\check{c} & \check{v}^T + \left(\|\check{v}\|^2/2 - \check{v}_{\eta_x}\right)\eta_x^T & \check{H} + \check{v}_{\eta_x}\check{c} \end{bmatrix}, \quad (\text{A.9})$$

and the left eigenvectors are

$$V_x(W_x, \eta_x)^{-1} = \frac{\check{\gamma} - 1}{2\check{c}^2} \begin{bmatrix} \|\check{v}\|^2/2 + \frac{\check{v}_{\eta_x}\check{c}}{\check{\gamma}-1} & -\check{v}^T - \frac{\check{c}}{\check{\gamma}-1}\eta_x^T & 1 \\ \frac{2\check{c}^2}{\check{\gamma}-1}(\check{v}_{\eta_x}\eta_x + \eta_x - \check{v}) - \|\check{v}\|^2\eta_x & 2\eta_x\check{v}^T + \frac{2\check{c}^2}{\check{\gamma}-1}(I_{d'} - \eta_x\eta_x^T) & -2\eta_x \\ \|\check{v}\|^2/2 - \frac{\check{v}_{\eta_x}\check{c}}{\check{\gamma}-1} & -\check{v}^T + \frac{\check{c}}{\check{\gamma}-1}\eta_x^T & 1 \end{bmatrix}, \quad (\text{A.10})$$

where $\check{c} = \sqrt{\gamma\check{P}/\check{\rho}}$.

Acknowledgments

This work is supported by AFOSR award numbers FA9550-20-1-0236, FA9550-22-1-0002, FA9550-22-1-0004, and ONR award number N00014-22-1-2299. The content of this publication does not necessarily reflect the position or policy of any of these supporters, and no official endorsement should be inferred.

References

- [1] Jude T. Anderson, David M. Williams, and Andrew Corrigan. Surface and hypersurface meshing techniques for space-time finite element methods. *Computer-Aided Design*, page 103574, 2023.
- [2] Randolph E Bank and Andrew H Sherman. An adaptive, multi-level method for elliptic boundary value problems. *Computing*, 26(2):91–105, 1981.
- [3] Garrett E Barter and David L Darmofal. Shock capturing with PDE-based artificial viscosity for DGFEM: Part I. Formulation. *Journal of Computational Physics*, 229(5):1810–1827, 2010.
- [4] Carlos E Baumann and J Tinsley Oden. A discontinuous hp finite element method for the Euler and Navier–Stokes equations. *International Journal for Numerical Methods in Fluids*, 31(1):79–95, 1999.
- [5] Marek Behr. Simplex space–time meshes in finite element simulations. *International journal for numerical methods in fluids*, 57(9):1421–1434, 2008.
- [6] J. B. Bell, G. R. Shubin, and J. M. Solomon. Fully implicit shock tracking. *Journal of Computational Physics*, 48(2):223–245, 1982.
- [7] Graham V. Candler, Michael Barnhardt, Travis Drayna, Ioannis Nompelis, David Peterson, and Pramod Subbareddy. Unstructured grid approaches for accurate aeroheating simulations. In *18th AIAA Computational Fluid Dynamics Conference*, Miami, Florida, June 2007. AIAA Paper 2006-3959.
- [8] Mark H. Carpenter and Jay H. Casper. Accuracy of shock capturing in two spatial dimensions. *AIAA Journal*, 37(9):1072–1079, September 1999.
- [9] Bernardo Cockburn and Chi-Wang Shu. Runge-Kutta discontinuous Galerkin methods for convection-dominated problems. *Journal of Scientific Computing*, 16(3):173–261, 2001.
- [10] Andrew T Corrigan, Andrew D Kercher, and David A Kessler. A moving discontinuous Galerkin finite element method for flows with interfaces. *International Journal for Numerical Methods in Fluids*, 89(9):362–406, 2019.

- [11] Andrew T Corrigan, Andrew D Kercher, and David A Kessler. The moving discontinuous Galerkin method with interface condition enforcement for unsteady three-dimensional flows. In *AIAA Scitech 2019 Forum*, page 0642, 2019.
- [12] Laslo T Diosady and Scott M Murman. Tensor-product preconditioners for higher-order space–time discontinuous Galerkin methods. *Journal of Computational Physics*, 330:296–318, 2017.
- [13] James Glimm, Xiaolin Li, Yingjie Liu, Zhiliang Xu, and Ning Zhao. Conservative front tracking with improved accuracy. *SIAM Journal on Numerical Analysis*, 41(5):1926–1947, 2003.
- [14] Peter Gnoffo. Simulation of stagnation region heating in hypersonic flow on tetrahedral grids. In *18th AIAA Computational Fluid Dynamics Conference*, Miami, Florida, June 2007. AIAA Paper 2007-3960.
- [15] Peter Gnoffo and Jeffery White. Computational aerothermodynamic simulation issues on unstructured grids. In *37th AIAA Thermophysics Conference*, Portland, Oregon, June 2004. AIAA Paper 2004-2371.
- [16] Ami Harten, Bjorn Engquist, Stanley Osher, and Sukumar R Chakravarthy. Uniformly high order accurate essentially non-oscillatory schemes, III. In *Upwind and high-resolution schemes*, pages 218–290. Springer, 1987.
- [17] Ami Harten and James M Hyman. Self adjusting grid methods for one-dimensional hyperbolic conservation laws. *Journal of Computational Physics*, 50(2):235–269, 1983.
- [18] Jan S Hesthaven and Tim Warburton. *Nodal discontinuous Galerkin methods: algorithms, analysis, and applications*. Springer Science & Business Media, 2007.
- [19] Tianci Huang, Charles Naudet, and Matthew J. Zahr. High-order implicit shock tracking boundary conditions for flows with parametrized shocks. *arXiv preprint arXiv:2304.11427*, 2023.
- [20] Tianci Huang and Matthew J Zahr. A robust, high-order implicit shock tracking method for simulation of complex, high-speed flows. *Journal of Computational Physics*, 454:110981, 2022.
- [21] Eric Johnsen, Johan Larsson, Ankit V Bhagatwala, William H Cabot, Parviz Moin, Britton J Olson, Pradeep S Rawat, Santhosh K Shankar, Björn Sjögren, Helen C Yee, et al. Assessment of high-resolution methods for numerical simulations of compressible turbulence with shock waves. *Journal of Computational Physics*, 229(4):1213–1237, 2010.
- [22] Andrew D Kercher and Andrew T Corrigan. A least-squares formulation of the moving discontinuous Galerkin finite element method with interface condition enforcement. *Computers & Mathematics with Applications*, 95:143–171, 2021.
- [23] Andrew D Kercher, Andrew T Corrigan, and David A Kessler. The moving discontinuous Galerkin finite element method with interface condition enforcement for compressible viscous flows. *International Journal for Numerical Methods in Fluids*, 93(5):1490–1519, 2021.
- [24] Christiaan M Klaij, Jaap JW van der Vegt, and Harmen van der Ven. Space–time discontinuous Galerkin method for the compressible Navier–Stokes equations. *Journal of Computational Physics*, 217(2):589–611, 2006.
- [25] Theodore Kai Lee and Xiaolin Zhong. Spurious numerical oscillations in simulation of supersonic flows using shock-capturing schemes. *AIAA Journal*, 37(3):313–319, March 1999.
- [26] Randall J. LeVeque. *Finite Volume Methods for Hyperbolic Problems*. Cambridge University Press, 2002.
- [27] Xu-Dong Liu, Stanley Osher, and Tony Chan. Weighted essentially non-oscillatory schemes. *Journal of Computational Physics*, 115(1):200–212, 1994.
- [28] Rainald Löhner. *Applied Computational Fluid Dynamics Techniques: An Introduction Based on Finite Element Methods*. John Wiley & Sons, 2008.

- [29] Robert B. Lowrie, Philip L. Roe, and Bram Van Leer. Space-time methods for hyperbolic conservation laws. In *Barriers and Challenges in Computational Fluid Dynamics*, pages 79–98. Springer, 1998.
- [30] William F Mitchell. 30 years of newest vertex bisection. In *AIP Conference Proceedings*, volume 1738, page 020011. AIP Publishing LLC, 2016.
- [31] Gino Moretti. Thirty-six years of shock fitting. *Computers & Fluids*, 31(4-7):719–723, 2002.
- [32] Maurizio Pandolfi and Domenic D’Ambrosio. Numerical instabilities in upwind methods: Analysis and cures for the “Carbuncle” phenomenon. *Journal of Computational Physics*, 166(2):271–301, January 2001.
- [33] P-O Persson and Jaime Peraire. Sub-cell shock capturing for discontinuous Galerkin methods. In *44th AIAA Aerospace Sciences Meeting and Exhibit*, page 112, 2006.
- [34] Per-Olof Persson. *Mesh generation for implicit geometries*. PhD thesis, Massachusetts Institute of Technology, 2005.
- [35] Per-Olof Persson. Shock capturing for high-order discontinuous galerkin simulation of transient flow problems. In *21st AIAA computational fluid dynamics conference*, page 3061, 2013.
- [36] Per-Olof Persson and Jaime Peraire. Sub-cell shock capturing for discontinuous galerkin methods. In *44th AIAA Aerospace Sciences Meeting and Exhibit*, page 112, 2006.
- [37] Jean-Christophe Robinet, Jérémie Gressier, Grégoire Casalis, and Jean-Marc Moschetta. Shock wave instability and the carbuncle phenomenon: same intrinsic origin? *Journal of Fluid Mechanics*, 417:237–263, August 2000.
- [38] Philip Roe, Hiroaki Nishikawa, Farzad Ismail, and Leonardo Scalabrin. On Carbuncles and other excrescences. In *17th AIAA Computational Fluid Dynamics Conference*, Toronto, Ontario, Canada, June 2005. AIAA Paper 2005-4872.
- [39] Philip L. Roe. Approximate Riemann solvers, parameter vectors, and difference schemes. *Journal of Computational Physics*, 43(2):357–372, 1981.
- [40] M.D. Salas. *A Shock-Fitting Primer*. CRC Press, 2009.
- [41] Andrew Shi, P-O Persson, and Matthew J Zahr. Implicit shock tracking for unsteady flows by the method of lines. *arXiv preprint arXiv:2101.08913*, 2021.
- [42] Andrew Shi, Per-Olof Persson, and Matthew J. Zahr. High-Order Implicit Shock Tracking (HOIST). In *Mesh Generation and Adaptation: Cutting-Edge Techniques*, pages 233–259. Springer, 2022.
- [43] Chi-Wang Shu and Stanley Osher. Efficient implementation of essentially non-oscillatory shock-capturing schemes, ii. *Journal of Computational Physics*, 83(1):32–78, 1989.
- [44] G. R. Shubin, A. B. Stephens, and H. M. Glaz. Steady shock tracking and Newton’s method applied to one-dimensional duct flow. *Journal of Computational Physics*, 39(2):364–374, 1981.
- [45] G. R. Shubin, A. B. Stephens, H. M. Glaz, A. B. Wardlaw, and L. B. Hackerman. Steady shock tracking, Newton’s method, and the supersonic blunt body problem. *SIAM Journal on Scientific and Statistical Computing*, 3(2):127–144, 1982.
- [46] JJ Sudirham, Jacobus JW van der Vegt, and Rudolf MJ van Damme. Space–time discontinuous galerkin method for advection–diffusion problems on time-dependent domains. *Applied numerical mathematics*, 56(12):1491–1518, 2006.
- [47] Eleuterio F. Toro. *Riemann Solvers and Numerical Methods for Fluid Dynamics: A Practical Introduction*. Springer Science & Business Media, 2013.

- [48] Bram Van Leer. Towards the ultimate conservative difference scheme. V. A second-order sequel to Godunov’s method. *Journal of Computational Physics*, 32(1):101–136, 1979.
- [49] J. Van Rosendale. Floating shock fitting via lagrangian adaptive meshes. Technical Report ICASE Report No. 94-89, Institute for Computer Applications in Science and Engineering, 1994.
- [50] G Vijayasundaram. Transonic flow simulations using an upstream centered scheme of Godunov in finite elements. *Journal of Computational Physics*, 63(2):416–433, 1986.
- [51] Max von Danwitz, Violeta Karyofylli, Norbert Hosters, and Marek Behr. Simplex space-time meshes in compressible flow simulations. *International Journal for Numerical Methods in Fluids*, 91(1):29–48, 2019.
- [52] Marcel Wallraff, Tobias Leicht, and Markus Lange-Hegermann. Numerical flux functions for Reynolds-averaged Navier–Stokes and $k\omega$ turbulence model computations with a line-preconditioned p -multigrid discontinuous Galerkin solver. *International Journal for Numerical Methods in Fluids*, 71(8):1055–1072, 2013.
- [53] Luming Wang and P-O Persson. A high-order discontinuous Galerkin method with unstructured space-time meshes for two-dimensional compressible flows on domains with large deformations. *Computers & Fluids*, 118:53–68, 2015.
- [54] Zhijian J Wang, Krzysztof Fidkowski, Rémi Abgrall, Francesco Bassi, Doru Caraeni, Andrew Cary, Herman Deconinck, Ralf Hartmann, Koen Hillewaert, Hung T Huynh, et al. High-order CFD methods: current status and perspective. *International Journal for Numerical Methods in Fluids*, 72(8):811–845, 2013.
- [55] Masayuki Yano. *An optimization framework for adaptive higher-order discretizations of partial differential equations on anisotropic simplex meshes*. PhD thesis, Massachusetts Institute of Technology, 2012.
- [56] Matthew J Zahr and P-O Persson. An optimization-based approach for high-order accurate discretization of conservation laws with discontinuous solutions. *Journal of Computational Physics*, 365:105–134, 2018.
- [57] Matthew J. Zahr and Per-Olof Persson. An r-adaptive, high-order discontinuous Galerkin method for flows with attached shocks. In *AIAA Scitech 2020 Forum*, page 0537, 2020.
- [58] Matthew J Zahr and Joseph M Powers. High-order resolution of multidimensional compressible reactive flow using implicit shock tracking. *AIAA Journal*, 59(1):150–164, 2021.
- [59] Matthew J Zahr, Andrew Shi, and Per-Olof Persson. Implicit shock tracking using an optimization-based high-order discontinuous Galerkin method. *Journal of Computational Physics*, 410:109385, 2020.